2015•2016
FACULTEIT INDUSTRIËLE INGENIEURSWETENSCHAPPEN
master in de industriële wetenschappen: nucleaire technologie

Masterproef

Quantitative capabilities of 2 state-of-the-art SPECT/CT imaging systems

Promotor :
dr. Brigitte RENIERS

Promotor :
Prof. dr. KRISTOF BAETE

Burak Yalvac

Scriptie ingediend tot het behalen van de graad van master in de industriële wetenschappen: nucleaire technologie

Gezamenlijke opleiding Universiteit Hasselt en KU Leuven

2015•2016

Faculteit Industriële ingenieurswetenschappen

master in de industriële wetenschappen: nucleaire technologie

Masterproef

Quantitative capabilities of 2 state-of-the-art SPECT/CT imaging systems

Promotor :
dr. Brigitte RENIERS

Promotor :
Prof. dr. KRISTOF BAETE

Burak Yalvac

Scriptie ingediend tot het behalen van de graad van master in de industriële wetenschappen: nucleaire technologie

universiteit hasselt | KU LEUVEN

Preface

The introduction of hybrid SPECT/CT imaging systems and the very recent development of three-dimensional (3D) iterative reconstruction algorithms made quantitative image analysis possible. This could make Standard Uptake Value (SUV) analysis possible for SPECT which is already the standard for Positron Emission Tomography (PET). These developments could make dosimetry in radionuclide therapy possible based on SPECT images corrected for attenuation, scatter and resolution recovery.
This thesis compares the quantitative capabilities of 2 state-of-the-art SPECT/CT imaging systems for Tc-99m in a clinical context for different acquisition and reconstruction parameters.
I hope that this work will provide insight for fellow researchers in quantitative image analysis and that it will contribute to the development of new techniques in nuclear medicine imaging.

This research would not been possible without the support of the following individuals.
I am very grateful to my external supervisor, prof. dr. Kristof Baete for his excellent guidance and training during my internship. He introduced me to the nuclear medicine department and trained me to use the various equipment in the department and how to operate the SPECT-CT systems.
I want to thank the department of Nuclear Medicine in UZ Leuven Campus Gasthuisberg for the access to the various equipment and also the technologists for their help and support.
I am very thankful to my internal supervisor, Brigitte Reniers PhD for her guidance and feedback on my research and thesis.
My special thanks go to Georg Schramm for his permission and training to use his script in my research.

Finally I want to thank my family and friends for their amazing and infinite support during my internship.

Contents

List of Tables

List of Figures

Vocabulary

FBP	Filtered Back Projection
HU	Hounsfield Units
LEHR	Low Energy High Resolution
MAP-EM	Maximum A Posteriori Expectation Maximization
NEMA	National Electrical Manufacturers Association
OS-EM	Ordered Subset Expectation Maximization
PMT	Photo Multiplier Tube
ROI	Region Of Interest
SPECT	Single Photon Emission Computed Tomography
$\mathbf{S_{vol}}$	System Volume Sensitivity
VOI	Volume Of Interest

Abstract

SPECT/CT using 3D iterative reconstruction techniques allows for the absolute quantification of radioactivity in vivo. This is essential for internal dosimetry in radionuclide therapy. The SPECT images are affected by attenuation, scatter and partial volume effects.
The goal of this study is to compare 2 state-of-the-art SPECT-CT systems (Siemens Symbia T16 and GE Discovery 670). The SPECT images were reconstructed using commercial iterative reconstruction algorithms. First, the systems were cross-calibrated with a radionuclide calibrator and a well counter using a large cylindrical phantom. Calibration factors (CF) were determined, converting image counts to activity concentration (kBq/ml). The influence of various acquisition and reconstruction parameters were investigated. Second, recovery values (RV) were determined for spheres with different diameters using the NEMA/IEC body phantom.
The quantitative accuracy in a large cylindrical phantom was 4%. The CF of the Symbia T16 and GE Discovery 670 were 11.59 cpm/kBq and 6.11 cpm/kBq, respectively. Oscillation and cupping artefacts were observed for the GE Discovery 670. The RV of the smallest spheres in the NEMA phantom dropped below 3.5% at 4 updates. The RV increased with the number of updates, but levelled at 64 updates. Quantification seems feasible within 4% for large objects. A partial volume correction technique is necessary for the smallest objects. The influence of reconstruction artefacts remains a challenge in SPECT/CT and should be the focus of further research.

Abstract

SPECT/CT met 3D iteratieve reconstructietechnieken maakt absolute kwantificatie in vivo mogelijk. Dit is essentieel voor interne dosimetrie in radionuclidetherapie. SPECT beelden worden beïnvloed door attenuatie, strooi- en partieel volume artefacten.
Het doel van deze studie is om 2 hedendaagse SPECT-CT systemen te vergelijken (Siemens Symbia T16 en GE Discovery 670). De SPECT beelden werden gereconstrueerd met commerciële iteratieve reconstructie algoritmen. De systemen werden eerst gekalibreerd met een radionuclide kalibrator en een gammateller met een cilindrische fantoom. Kalibratie factoren (CF) werden bepaald om image counts te converteren naar activiteit concentratie (kBq/ml). De invloed van diverse parameters werden onderzocht. Ten tweede werden Recovery values (RV) bepaald voor sferen met verschillende diameters gebruik makend van het NEMA/IEC body fantoom.
De kwantitatieve nauwkeurigheid in een brede cilindrische fantoom was 4%. De CF van Symbia T16 en GE Discovery 670 waren respectievelijk 11.59 cpm/kBq en 6.11 cpm/kBq. Oscillatie en cupping artefacten werden waargenomen voor GE Discovery 670. De RV's van de kleinste sferen in het NEMA fantoom vielen onder 3.5% bij 4 updates. De RV steeg met meer updates, maar werden stabiel bij 64 updates. Kwantificatie lijkt realiseerbaar met 4% voor grote objecten. Een techniek voor partieel volume correctie is nodig voor de kleinste objecten. De invloed van reconstructie artefacten blijft een uitdaging voor Q-SPECT en hierop zouden verdere onderzoeken zich moeten focussen.

1 Introduction

Single Photon Emission Computed Tomography (SPECT) is a non-invasive tomographic imaging technique within the nuclear medicine and molecular imaging. It is used to image biological activity where the patient is injected with a gamma-emitting radionuclide (mostly ^{99m}Tc). The emitted gamma rays within the patient are collected by gamma cameras which rotate around the patient and this information is used to reconstruct a 3D image. Current clinical diagnosis is based on image reconstructed pixel intensities which do not represent the true activity concentration in the scanned object [1]. Thanks to recent developments of Hybrid SPECT/CT systems with 3D iterative reconstruction algorithms and the increase in computing power made it possible for SPECT to exactly quantify the concentration of radioactivity within a given volume of tissue in absolute units e.g. kBq/cm^3. Unfortunately this is compromised by photon scattering, attenuation, partial volume and motion artefacts [2]. Accurate quantification could lead to interesting developments like determining the exact amount of tracer uptake in the patient, or to perform dosimetry in radionuclide therapy with beta-emitters (e.g. Y-90 microspheres for liver cancer) [3]. To achieve these objectives the SPECT/CT imaging systems must be calibrated in absolute units instead of pixel intensities. This requires the calculation of a calibration factor which converts pixel intensity (counts/voxel) to absolute units (kBq/ml) [4].
The aim of this study is to compare the quantitative capabilities of the following state-of-the-art SPECT/CT imaging systems for the use of clinical Tc-99m:

- Siemens Symbia T16
- General Electric Discovery NM/CT 670

This was accomplished by scanning of physical phantoms and examining the influence of various acquisition and reconstruction parameters. The images were reconstructed using the vendors own commercial 3D iterative reconstruction algorithms (Siemens Flash3D and GE Evolution for Bone) and a vendor neutral commercial reconstruction algorithm (Hermes Hybridrecon).

Chapter 2 gives an introduction of SPECT/CT technology and quantitative SPECT reconstruction. Chapter 3 describes the materials and methods used in this project. Chapter 4 and 5 shows the results of both imaging systems and compares Hermes Hybridrecon to the manufacturers results. Chapter 6 discusses the results in the previous 2 chapters.
Chapter 7 deals with the personal reflection and experiences during the internship and chapter 8 gives the final conclusion of this research.

2 SPECT/CT technology

SPECT/CT imaging systems consists of 1 (or more) gamma cameras and a CT-scanner integrated on the same gantry. Both imaging devices can be operated independently. The SPECT/CT acquisition is performed sequentially. The SPECT acquisition is often acquired before the CT acquisition (depending on the examination). Before the CT acquisition, the patient needs to be moved to the correct position for the CT-scan by an axial table movement. This is to ensure proper co-registration of the images. After the acquisition, the fused SPECT/CT image can be viewed which combines the advantages of both imaging modalities. SPECT/CT provides a substantial advantage as compared to SPECT solely. The CT image is used for attenuation correction (by generating an attenuation map) and also for localization of anomalies and anatomical information [5].

2.1 Gamma (Anger) camera

The gamma camera is a device that detects photons. It consists of a flat scintillator block of NaI with a thickness of typically 3/8 (0.95 cm) or 5/8 inch (1.58 cm). One side of the crystal is completely covered by an array of Photo Multiplier Tubes (PMT). The other side is facing the object to be scanned through a collimator (mostly parallel hole) which limits the direction of the incoming photons to (almost) perpendicular to the face of the camera [6]. Figure 2.1 shows an illustration of the gamma camera.

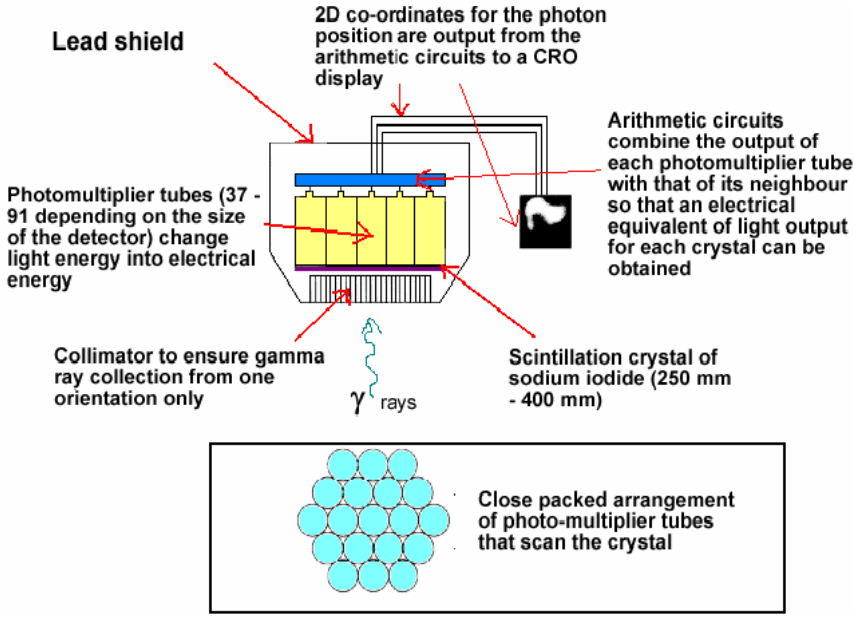

Figure 2.1: Illustration of a gamma camera [7]

2.1.1 Photo Multiplier Tube

Photomultipliers are typically constructed with an evacuated glass housing, which contains a photocathode, several dynodes, and an anode. When photons collide with the NaI crystal, the gamma ray photons are converted to light. When this light strikes the photocathode of the PMT, the light is converted to electrons by photoelectric absorption. The number of electrons created is proportional to the amount of radiation received by the crystal. These electrons are directed by the focusing electrode toward the electron multiplier, where electrons are multiplied by the process of secondary emission. The electron multiplier consists of dynodes, where the initial electrons are multiplied with a factor of approximately 10^5. At the anode the multiplication results in an electrical pulse which can be analysed and yields information about the energy and the position of the particle that originally struck the scintillator [8].

A gamma camera consists of an array of PMT (about 60) which covers one side of the NaI crystal. The energy and position of the detected photons is calculated by pulse height spectrometry and by analysing differences in signals recorded by many photo-multipliers [8]. Figure 2.2 gives an illustration of a PMT.

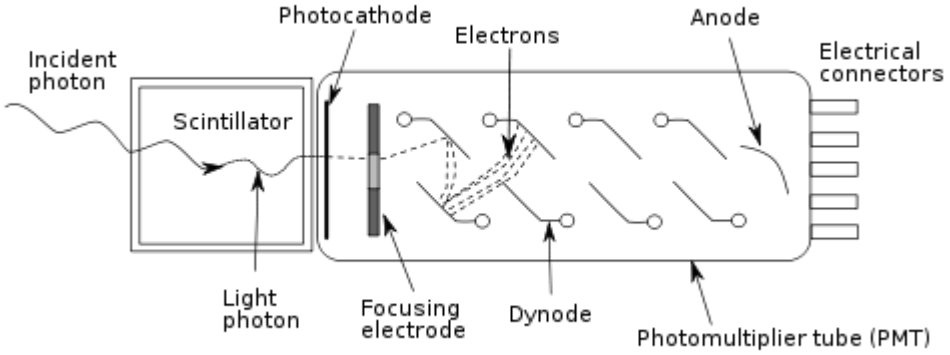

Figure 2.2: An illustration of a PMT [9]

2.1.2 Collimator

The collimator is mounted on the gamma camera. Its function is to limit the field of view so that γ-radiations from outside the field of view are prevented from reaching the detector. The collimator consists of several rows of septa made from lead (or tungsten) with holes between. The thickness of the septa is related to the energy of the radionuclide injected to the patient. SPECT applications typically make use of parallel hole collimators in order to establish an orthogonal detection geometry with the crystal detectors. The collimation reflects the compromise between sensitivity and spatial resolution. The resolution of the gamma camera is primarily limited by the geometric resolution of the collimator, which is of the order of 6–9 mm at a distance of 10 cm from the collimator. Table 2.1 shows the most commonly used collimators in clinical practice [10].

Table 2.1: Performance of commonly used collimators in nuclear medicine [10]

Collimator type	Gamma energy (keV)	Efficiency	Resolution at 10 cm (mm FWHM)
LEHR	150	1.8×10^{-4}	7.4
LEGP	150	2.7×10^{-4}	9.1
LEHS	150	5.8×10^{-4}	13.1
MEHS	400	1.7×10^{-4}	13.4

LEHR: Low Energy High Resolution
LEGP: Low Energy General Purpose
LEHS: Low Energy High Sensitivity
MEHS: Medium Energy High Sensitivity

Imaging of low-energy radionuclides is generally limited to the use of general purpose, parallel hole collimators. The development of multi-head cameras and the resulting increase in sensitivity made it possible to improve spatial resolution by the use of high-resolution collimators, which nowadays is the standard in most clinical applications [11].

2.2 SPECT acquisition

Before the SPECT acquisition starts, a radioactive tracer (gamma-emitter) is injected in the patient and the patient waits for a considerable time which is dependent on the tracer and the examination (sometimes more than 30 min.) until the activity is distributed within the body. Tc-99m is mostly used in SPECT modalities [3].

Figure 2.3. shows the principle of SPECT acquisition.

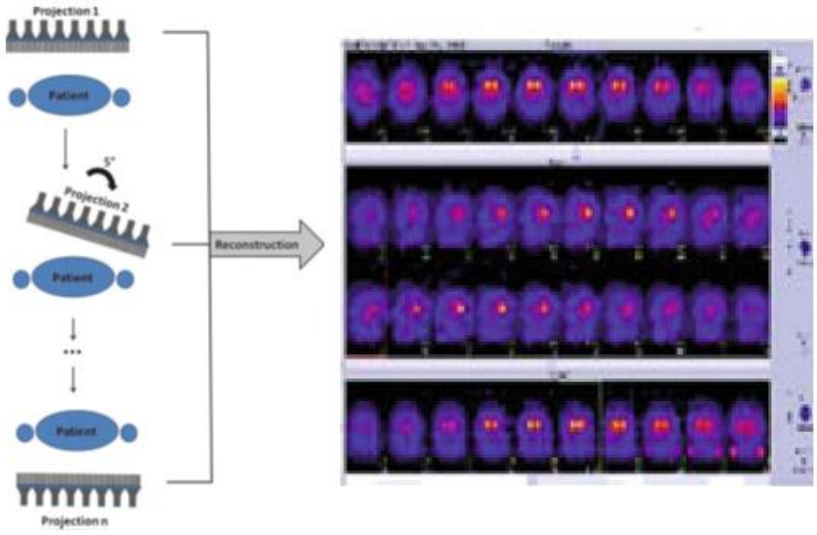

Figure 2.3: Principle of conventional SPECT data acquisition with a rotating gamma camera [10].

The gamma camera rotates around the patient while the camera acquires 2D-projections of the radioactivity distribution at different angles (e.g. an angular step of 3°). Modern gamma cameras have the capability for elliptical orbits by equipping the collimators with sensors that can detect the presence of the patient. This allows for the camera head(s) to maintain in close proximity of the patient during the acquisition. Since the spatial resolution of the system degrades with increasing distance of the camera heads from the patient, it is important that the camera head(s) stays as close as possible to the patient. A 360° rotation is desirable for most clinical studies. Each projection is acquired for a variable time. The camera remains still during the acquisition of each planar projection (Step-and Shoot) or the camera still collects photons during the rotation to another projection angle (continuous). This process can be accelerated with multi-headed systems e.g. a dual headed camera with heads spaced 180° apart (H-mode) allows two projections to be acquired simultaneously. Hereby each camera head needs to rotate 180° for a total view of 360°. To obtain a useful image, an energy discriminator is used i.e. only photons with an energy in that range will be detected. An energy window of 10-20% around the energy of the radionuclide (e.g. 140 keV for Tc-99m) is commonly used in clinical practice [5], [6], [11]. For most SPECT applications, the acquisition matrix size for acquiring planar projection images is typically a 128 x 128 array. The decision is based on the size of the smallest object to be imaged in the distribution being studied [10].

2.3 Quantitative SPECT Reconstruction

The next step after the SPECT and CT acquisition is to reconstruct a 3D image.
A SPECT image shows the count distribution as a stack of 2D transaxial images. SPECT also has the potential to exactly quantify the count profile in absolute units of radioactivity within a given volume e.g. (kBq/cm³). However, to accurately quantify the SPECT images, corrections must be applied for attenuation, scatter, partial volume artefacts and patient motion.
Iterative reconstruction techniques have proven to be superior than Filtered Back Projection (FBP) for quantification where corrections for physical artefacts can be incorporated in the iteration process [12]. Iterative reconstruction starts with a first estimation of the image which is mostly a uniform activity distribution. Then, this estimation is forward projected. Next, the projections of the estimated image are compared with the real projections. Finally, the results are used to update the current estimation. This process is repeated until the estimated image converges to the actual image within a defined criteria [1], [11], [12].
Shepp and Vardi introduced an iterative reconstruction technique in 1982 based on the theory of expectation maximization (EM) [13], which has a proven theoretical convergence to an estimate of the actual image distribution that has a maximum likelihood of having projections most similar to the acquired projections. Initially, the implementation of these algorithms was very time consuming because extensive computer power was required. Today, the advances in computer technology and the improvements of these algorithms make it possible to use iterative reconstruction techniques in clinical practice [11], [14].

Nowadays, the technique of Ordered Subsets EM (OS-EM) is used mostly in clinical practice. In OS-EM the projection data is divided into small subsets where the EM algorithm is performed on each subset [15]. The solution of each subset is used as the starting point (estimated image) for the next subset. This has the advantage that when the entire projection data is processed, the image has been updated n times where n is the number of subsets. Most commercial algorithms also use post-filtering to reduce the noise in the image [6], [11], [12]. The following sections will discuss the most important physical artefacts that degrade the quantitative accuracy of SPECT images.

2.3.1 Attenuation correction

SPECT images are largely affected by photon attenuation. The photons are attenuated in the body because of photoelectric absorption and Compton scatter. Compton scattering is the predominant type of interaction clinically. Photoelectric absorption results in a complete removal of the photon from the radiation field, while Compton scattering results in a change in direction with loss of photon energy where the magnitude of the loss is determined by the angle of scatter [10]. Figure 2.4 shows the difference between an uncorrected and corrected SPECT image of a uniform cylindrical phantom. Notice the large cupping artefact (more visible in the line profiles) due to photon attenuation in the centre of the uncorrected image.

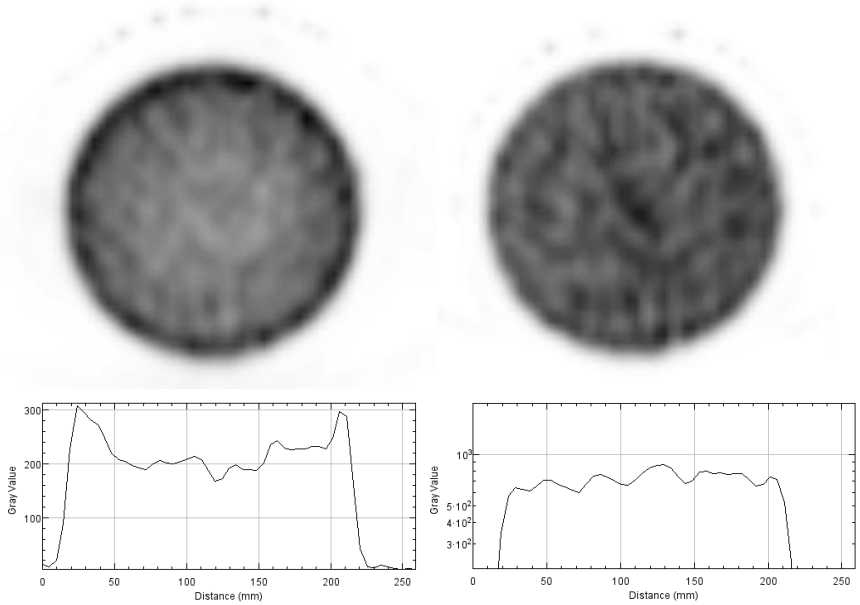

Figure 2.4: Difference between a uncorrected and corrected SPECT image. Left: uncorrected. Right: Corrected (from Symbia T16)

To correct for attenuation effects, the spatial distribution of the attenuation coefficients of the examined object for the photon energy of the radionuclide used needs to be known [2]. Thanks to the development of hybrid SPECT/CT imaging systems, it is now possible to generate the attenuation maps through a transmission scan of the patient (e.g. a CT-scan). Two reconstructions are made from the CT scan: one reconstruction is used for fused image viewing while another reconstruction with smooth kernels (the resolution is deliberately lowered) is used for attenuation correction for the SPECT image. The CT scan is converted

from Hounsfield Units (HU) to linear attenuation coefficients (units of cm^{-1}) at the respective photon energy [16].
The transformation of the CT image to attenuation coefficients at the effective energy of the SPECT scan can introduce errors. First, the transformation is specific for different acceleration voltages and beam filters of the CT scanner [11].
Secondly, the polychromaticity of the X-ray beam also introduces artefacts which are mainly caused by beam hardening. Patient motion that occurs during the acquisitions can lead to incorrect co-registration and fusion of the SPECT and CT images. This will result in an incorrect attenuation map and a false correction for attenuation. Besides, diagnosis will be difficult because of the incorrect fusion of both images.
The conversion of HU is typically accomplished by using a bilinear model relating attenuation coefficients at the desired energy to CT numbers measured at the effective energy of the X-ray beam. Figure 2.5 shows the bilinear model used for the conversion. The parameters of the transformation are defined by the linear attenuation coefficients for air, bone and water at the respective photon energies [5], [10].

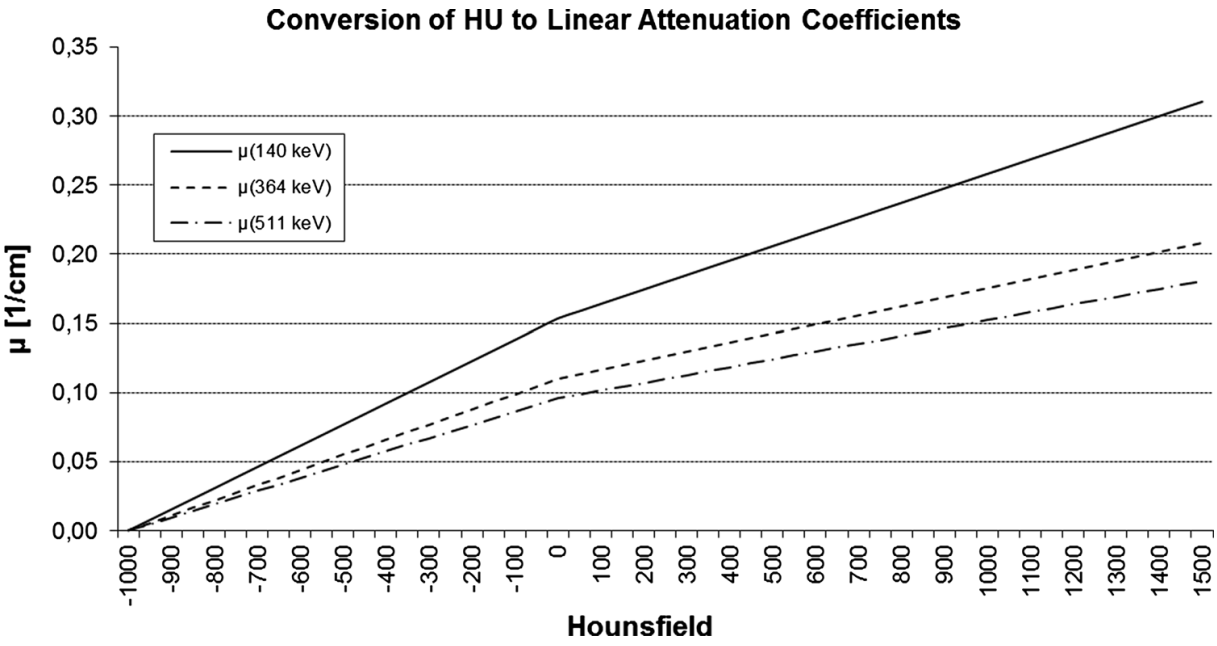

Figure 2.5: Bilinear model used for conversion of Hounsfield Units into linear attenuation coefficients [5].

2.3.2 Scatter correction

Another major factor which degrades image quality is photon scatter. The Compton effect is the pre-dominant process of scattering in the patient where the amount of energy loss depends on the scatter angle. The photo peak window of a SPECT acquisition is about 15-20%. This means that some of the photons that have been scattered in the patient with a small deflection angle (small loss of energy) will therefore have a possibility to be detected within such a large energy window. These photons carry wrong spatial information about the decay location in the object. This will result in a degraded image contrast and problems for accurate quantification [10].
There are numerous methods for scatter correction. The earliest method is the use of a lower energy window (adjacent to the photo peak window) to measure a scatter image. The

underlying premise is that the scatter image, scaled by an appropriate factor, k, provide an estimate of the scatter contribution that degrades the photo-peak window image [17].
Another method is the use of a Triple Energy Window (TEW) method proposed by Ichihaa [18]. In this method the third adjacent window is used to estimate the upper scatter. Often the upper limit window is set to zero.
The scatter images are acquired simultaneously with the photopeak image. For each pixel of the projection image, the amount of scattered radiation in the photopeak window image is estimated from the scatter window images. This amount can be subtracted from the projections or incorporated into the iterative reconstruction algorithm [5], [12].
Yet another method for scatter correction is based on Monte Carlo (MC) calculations. In this method, a MC simulation is used as a forward-projector for scatter in the OS-EM algorithm. This is expected to be especially advantageous in areas where the attenuating media is highly non-uniform such as the thorax, because it can reproduce the complex shape of the scatter response function [19].
More detailed information about SPECT scatter techniques can be found in Hutton et al. [20].

2.3.3 Depth dependent resolution recovery

Compensation for the degradation in spatial resolution due to the collimator-detector response Function (CRF) improves spatial resolution and is necessary for the quantification of SPECT images [2]. The collimator-detector response function consists of 4 parts which degrades spatial resolution.
The first part is the intrinsic response of the detector which is dependent of the structure and thickness of the crystal (e.g. thicker crystals increase the detector efficiency but they decrease the intrinsic resolution). It is characterized by the intrinsic response function which can be incorporated in the iteration process [1].
Second, the sensitive volume of one collimator hole is more cone-shaped than cylindrical shaped. As a result, the system resolution of a point source depends (approximately) linearly on the distance between the source and detector for a gamma camera with parallel hole collimators. This effect is known as the geometric response function, and a mathematical model for this can easily be incorporated into the iteration process [21].
The third factor which degrades image quality is septal penetration. Thicker septa reduce the amount of septal penetration, but they also reduce the efficiency by covering more sensitive area of the detector. As a compromise, a certain amount of septal penetration is allowed. Septal penetration can be described by the mathematical septal penetration function which can be incorporated in the iteration process [5].
The fourth possible interaction which degrades image quality is septal scatter. When photons interact with a collimator septa, normally it should be stopped by the septa. But it is possible that some photons get deflected by the collimator septa and still reach the detector. These photons no longer carry correct information about the object location because of this deflection. The probability that photons are scattered by the septa is modelled by the septal scatter function which can be incorporated in the iteration process [2].
Figure 2.6 shows an illustration of the 4 parts which form the collimator-detector response function.

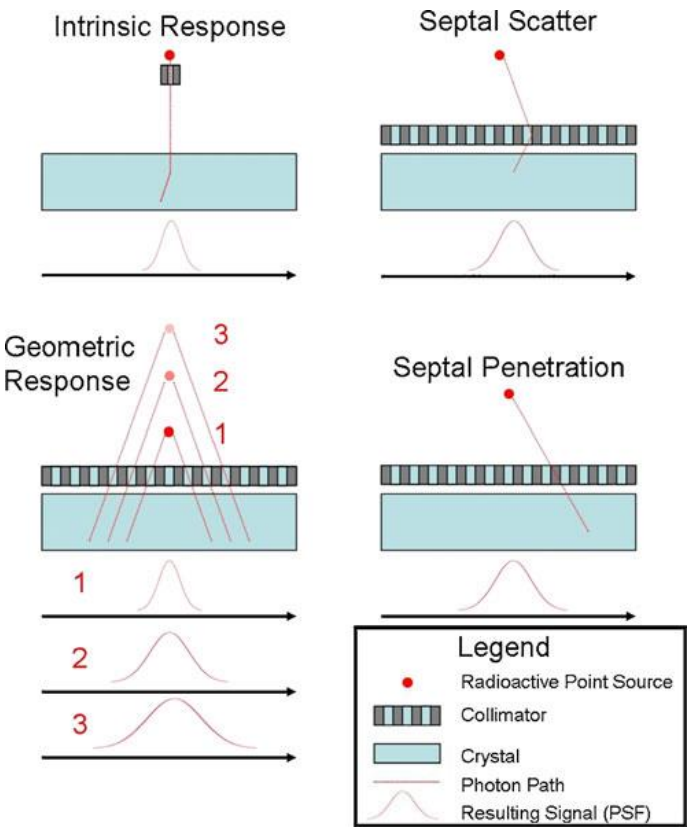

Figure 2.6: Illustration of the 4 parts of the collimator-detector response function [2]

Instead of reconstructing each axial slice independently, the interslice blurring caused by the described processes above is taken into account during both forward and back projection steps of the iteration process [12]. This significantly increases the computational time, but it allows that the reconstructed image has a "higher" resolution than the acquired projection images, hence the name "resolution recovery" [2]. The increase of the system resolution will also minimize Partial Volume (PV) effects which is discussed in the next section.

2.3.4 Partial volume correction

Partial volume artefacts are caused by the limited spatial resolution of SPECT imaging devices. Regions of interest (ROI's) in structures with heterogeneous activity distribution below approximately twice the spatial resolution are degraded: Their activity is either under- or over-estimated which depends on the combination of "spill-in" and "spill-out". Spill-in happens in cold spots (small regions with low activity) which resides in a hot background (high activity). It refers to the effect that activity from outside the ROI is integrated into the ROI and therefore the activity inside the ROI is increased.
Spill-out happens in hot spots (small regions with high activity) which resides in a cold background (low activity). It is understood as the activity of the ROI/structure is distributed over the borders and therefore the activity inside the ROI is decreased. Therefore the accuracy for quantification is lost significantly (e.g. the measured activity of a small tumour is underestimated due to spill-over). The degree of the partial volume effect depends on the (spatially varying) system resolution of the imaging system, the patient (e.g. motion), and the true distribution of radioactivity in the image. Any methods used for the improvement of the

spatial resolution (which was discussed in the previous section) will also decrease partial volume artefacts.
One method for partial volume correction can be applied in experiments with physical phantoms. It is possible to calculate recovery coefficients (measured activity concentration to true activity concentration) for small geometrical structures. A known limitation of this method is that this method only applies for simple geometries like circles [2], [22]. Another limitation is that this method only applies to scanned objects which remain still during the acquisition (i.e. phantoms).

2.3.5 Cross calibration

The calibration of the SPECT imaging system volume sensitivity S_{Vol} (e.g. in cpm/kBq) is the final requirement for absolute quantitative imaging. The S_{Vol} allows to convert the measured count distribution (cpm/voxel) to units of absolute activity (kBq/cm^3). This is typically obtained by a correlation of the results with an ionization chamber and a radionuclide calibrator. The reading of the ionization chamber is multiplied by the calibration value (nuclide specific) of the radionuclide calibrator which then gives the amount of activity (this is used to measure the activities in clinical practice before the patient is injected). Besides, a well counter is used for Quality Assurance (QA) of the ionisation chamber.
The calibration factor is specific for every radionuclide, amount of activity as well as to different system sensitivities. It is also dependent on the ionisation chamber used to measure the activity [12].

3 Materials and Methods

3.1 Imaging systems

The Siemens Symbia T16 and GE Discovery NM/CT 670 are state-of-the-art SPECT/CT imaging systems with dual head detectors. Table 3.1 shows the important system specifications of both systems and Table 3.2 shows the main specifications of the commercial 3D iterative reconstructions methods. Table 3.3 shows the main characteristics of the Low Energy High Resolution (LEHR) collimators of both manufacturers.

Table 3.1: Main specifications of both SPECT/CT systems used in the study [22]

Name	SPECT detector	NEMA spatial resolution* with LEHR collimator (mm)				CT
		Planar	SPECT Central	SPECT Peripheral		
				Radial	Tangential	
General Electric Discovery NM/CT 670	3/8 in. NaI crystal 59 PMT 1 ADC/PMT 40 × 54 cm FOV	7.4	≤9.9	≤9.9	≤7.5	80, 100, 120, and 140 kV 10 to 440 mA 0.5, 0.6, 1.0, and 1.5 s rotation time (in spiral mode) 24 rows - maximum 16 slices/rotation
Siemens Symbia T series	3/8 in. NaI crystal 59 PMT 38.7 × 53.3 cm FOV	7.4	≤11.4	≤11.7	≤8.4	80, 110, and 130 kV T16: 20 to 345 mA; 0.5, 0.6, 1.0, and 1.5 s rotation time; 24 rows - maximum 16 slices/rotation

Table 3.2: Main characteristics of the 3D iterative reconstruction algorithms [22]

Name	Type	Corrections			Noise regularization	Manufacturer default number of	
		Attenuation	Scatter	Resolution		Subsets	Iterations
General Electric Evolution for Bone	MAPEM	From CT data, bilinear conversion of HU into attenuation coefficients at 140 keV	Jaszczak's dual energy window method with 115 to 125 keV scatter window	Matrix rotation Row convolution with spatial resolution kernel stored in look-up table	One-step late method with green prior and median root prior at last iteration	10	2
Siemens Flash 3D	OSEM	From CT data, bilinear conversion of HU into attenuation coefficients at 140 keV	Modified triple energy window method with 108.5 to 129.5 keV scatter window	Matrix rotation Gaussian diffusion method with slabs	Gaussian post-filter (6-mm FWHM default value)	4	12

Table 3.3 Main characteristics of the LEHR collimators

LEHR collimator		
Parameter	**Symbia T16**	**Discovery NM/CT 670**
Hole shape	Hex	Hex
Hole length	24.05 mm	35mm
Septal Thickness	0.16 mm	0.2mm
Hole Diameter Across the Flat	1.11mm	1.5mm
Sensitivity @ 10cm	202 cpm/µCi	160 cpm/µCi
Septal Penetration	1.5 %	0.3%

Even though the commercial SPECT/CT systems and 3D reconstruction algorithms of both manufacturers have common features, they also have differences. The SPECT component uses similar technologies still based on the 50-year-old Anger camera. Furthermore, the number of photomultiplier tubes, the planar spatial resolution, the fields of view and the CT component are approximately identical. However, the LEHR collimators are different. The Discovery NM/CT 670 has longer holes and thicker septa which reduces image noise but reduces the sensitivity.

Both manufacturers use the bilinear transformation technique to convert the HU to attenuation coefficients based on the work of Fleming [16]. It is likely that the implementation by the two manufacturers is different.

Both vendors use different approaches for scatter correction. General Electric uses the Dual Energy Window (DEW) method (second broad low energy window) suggested by Jaszczak [17] which is used to estimate the scatter in the photopeak window. Siemens scatter correction is based on the triple energy window (TEW) method [18]. Often, the upper limit is set to "zero" which makes it basically a modified DEW method. The scatter is estimated from a unique lower energy window that is adjacent to the main window and has the same width, and not from the two very narrow energy windows of the original TEW. The scatter data is not subtracted from the main energy peak projections but is used in the iterative reconstruction loop.

Both vendors use resolution recovery in their OS-EM algorithm. Because resolution recovery considerably increases the computing load, some accelerating schemes are used. The 3D image matrix is first rotated in a way that the transverse slices have rows parallel to and columns perpendicular to the camera detector. The spatially variant camera resolution is taken into account in both the forward- and back-projection steps of both algorithms [22].

General Electric Evolution for Bone is based on the work done at the University of North Carolina and Johns Hopkins University [23], [24]. After the matrix rotation, each row is convoluted with a kernel stored in look-up tables that describe the spatial response of the camera at this distance [22].

Siemens Flash3D makes use of the Gaussian diffusion method. After the matrix rotation, the slice row farthest from the detector is convoluted with a Gaussian function that describes the difference in spatial resolution between this row and the adjacent row. This result is added to the adjacent row, and the process is repeated. The steps are reversed in a back-projection. In

order to proceed even faster, rows are grouped into slabs [25], and the process described above is applied to these slabs [22] and not the individual rows.
Both algorithms also make use of noise regulation. Flash3D makes no noise regularization during the iterations. Instead, Noise control is performed after the last iteration with a Gaussian filter (post-filter) whose width can be adjusted by the user.
GE Evolution uses a Maximum A Posteriori Expectation Maximization (MAP-EM) type. Noise regularization is accomplished by applying a penalty to the image resulting from the previous iteration following the one-step late method proposed by Green [22], [26].

SPECT reconstructions were made with the Flash3D algorithm (on the Syngo 2009A workstation) for the Symbia T16, GE Evolution for Bone algorithm (on the Xeleris 3.0 and Xeleris 3.1 workstation) for the Discovery NM/CT 670.

3.1.1 Hermes Hybridrecon

Besides the vendors own commercial algorithms to reconstructs images, the Hermes Hybridrecon Oncology algorithm was also used to make SPECT reconstructions. The Hermes Hybridrecon is a vendor neutral reconstruction algorithm which makes SPECT reconstructions by taking physical information into account (e.g. camera size, collimator properties) provided from different vendors.
Hermes Hybridrecon uses a 3D iterative reconstruction algorithm comparable to the Flash3D and GE evolution algorithm. However, Hybridrecon uses a Monte Carlo Simulation method [19] for the scatter correction instead of the spectral based techniques used by the vendors algorithms.

3.2 Activity measurements

All activities were carefully measured with the radionuclide Calibrator Capintec CRC-55tR where the time of measurements was recorded. The radionuclide calibrator was adjusted for the measurement of Tc-99m. The calibrator has an accuracy of 2% (as stated by the manufacturer). The radionuclide calibrator undergoes a daily quality control.
Also, samples of 1 ml inside the phantom were taken with a calibrated pipette of 1ml (Thermo fixed pipette 1ml). These samples were read out on a well counter (Perkin Elmer Wallac 1480 well counter) which has an accuracy of 1%. The volume of the samples were determined by weighing the samples on a scale (Sartorius CP124S). The density of distilled water was taken as 0.998 g/cm^3. This was used as an extra measurement to control the measurements of the dose calibrator and the gamma camera's.

3.3 Image processing

These software were used for processing of the reconstructed images.

- HERMES Hybrid Viewer (PDR 2.5A)
- ImageJ

The Regions Of Interest (ROI's) were first drawn on the CT image and then these ROI's were translated to the SPECT image. Microsoft EXCEL was used to perform calculations on the ROI data obtained from the various processing software.

3.4 Quantification

The S_{Vol} was calculated using a uniform cylindrical phantom with a volume of 6283 ml (height 20 cm, diameter 20 cm). The cylindrical phantom contains a metal stir rod for helping to achieve a uniform activity distribution. The phantom is filled with distilled water. The Tc-99m activity was measured in the Capintec CRC-55tR well counter before being introduced into the phantom.
The phantom was measured on both imaging systems. The images were acquired in H-mode (both detectors 180° apart) with LEHR collimators. Each detector had a rotation arc of 180° with an angular step of 3°. The time per projection (dwell time) was 10 seconds. This gave 60 views in total and a scanning time of 10 minutes. The detectors had a non-circular orbit (i.e. the detectors were as close as possible to the scanned object). The detector motion was continuous for the Symbia T16 and Step and Shoot[1] for the discovery. Both the photopeak and scatter window were set to 15%[2]. This resulted in the following values:

- Symbia T16
    - Photopeak window: 128.7-149.6 keV
    - Scatter window: 108.5-128.5 keV
- Discovery NM/CT 670
    - Photopeak window : 130-151 keV
    - Scatter window: 109-126 keV

The pixel size for the Symbia T16 and Discovery NM/CT 670 were 4.8 mm and 4.4 mm respectively. The activity during the time of acquisition was around 500 MBq. The attenuation map was generated by a CT-scan. For the Symbia T16,
the CT-scan was done with 130 kV and 30 mAs with both a smooth and medium reconstruction kernel (B08 and B30 respectively) with slice thicknesses of 5 mm and 1.5 mm respectively. For the Discovery NM/CT 670, the CT-settings were 120 kV, 20 mAs and both a smooth and medium reconstruction kernel with slice thicknesses of 5 mm and 1.25 mm. The images were reconstructed using Flash 3D for the Symbia T16 and GE Evolution for Bone for the Discovery NM/CT 670.
The GE evolution for Bone algorithm contains a projection counts multiplication factor of 4 to improve image quality with low counts. It is important to turn this feature off for quantification purposes.

[1] The Xelerix 3.0 Workstation does not allow for an acquisition where the detector motion is continuous and the orbit is non-circular.
[2] First, the scatter window of the Discovery NM/CT 670 was 10%. But in the following measurements the scatter window was adjusted to 15% to be the same as the scatter window of the Siemens Symbia T16.

Flash3D was used with 6 subsets and 15 iterations with a post-smoothing of 7.5mm. GE Evolution for Bone was used with 10 subsets and 6 iterations with a post-smoothing penalty of 2 pixels value. These settings were chosen as the "standard". Other measurements with different parameters were compared to these settings.
Reconstructions were also made with the Hermes Hybridrecon Oncology algorithm were the settings were identical to the Flash3D and GE evolution for Bone except the scatter correction which is based on MC simulation. An energy window of 10% is used for the scatter correction.
The S_{Vol} was calculated by first drawing a large volume of interest (VOI) in the uniform part of the in the reconstructed image and then calculating the decay-corrected counting rate $\hat{R}$ with equation (1) [27] :

$$\hat{R} = R \exp\left(\frac{T_0 - T_{cal}}{T_{1/2}}\ln 2\right)\left(\frac{T_{acq}}{T_{1/2}}\ln 2\right)\left(1 - \exp\left(-\frac{T_{acq}}{T_{1/2}}\ln 2\right)\right)^{-1} \quad (1)$$

With:

R: Count rate derived from the reconstructed image (cpm)
T_0: Start time of the acquisition (hh:mm:ss)
T_{cal}: Time of the activity calibration (hh:mm:ss)
$T_{1/2}$: The half-life of the radionuclide (min.)
T_{acq}: The time duration of the acquisition (min.)

The first term in brackets corrects for the radioactive decay from the time of calibration until the start time of the acquisition. The second term corrects for the duration of the acquisition and the third term calculates the mean counts considering an exponential decay during acquisition [27].
The system volume sensitivity follows from equation (2):

$$S_{Vol} = \frac{\hat{R}/V_{VOI}}{c_A}, \quad (2)$$

With:
$\hat{R}$: Decay corrected count rate (cpm)
V_{VOI}: The volume of the drawn VOI (cm^3)
C_A: Actual activity concentration in the phantom at T_{cal} (kBq/cm^3)

The unit of the system volume sensitivity is cpm/kBq.

Besides, 3 samples of 1 ml of the concentration were measured in the well counter. The results of the samples in the well counter are given in Appendix A: Well counter results.

3.4.1 Uniformity analysis

The uniformity of the reconstructed images was examined by taking Region Of Interests (ROI's) in all the slices (inner 80% of the phantom) and plotting the mean, min and maximum counts. The counts were converted to absolute units (kBq/ml) by dividing the count density by the S_{vol}.

3.4.2 Influence of number of updates

The influence of the number of updates (number of subsets x number of iterations) was examined by making different reconstructions. The number of updates was varied from 4-120 updates. The other acquisition settings were identical to those described in 3.4.
Table 3.4 shows the number of updates used in this study.

Table 3.4: Various number of updates used in this study

Subsets	Iterations	Updates
2	2	4
2	4	8
4	4	16
4	8	32
8	8	64
10	12	120

3.4.3 Influence of pixel size

The influence of the pixel size on the System Volume Sensitivity (S_{vol}) was examined by varying the pixel size from 2mm-9mm. The other acquisition settings were identical to those described in 3.4. Table 3.5 shows the pixel sizes used.

Table 3.5: Pixel sizes used in this study for the influence on the S_{vol}

Pixelsize (mm)	
Symbia T16	Discovery NM/CT 670
2.40	2.21
4.80	4.42
9.59	8.83

3.4.4 Influence of activity

The influence of the amount of activity was examined by varying the activity between 20-500 MBq. The other acquisition settings were identical to those described in 3.4 except for the

measurement with very low activity (<30MBq), the dwell time (time per projection) was 30 seconds instead of 10 seconds to obtain good count statistics.

3.4.5 Influence of detector motion and orbit

The influence of the detector motion and orbit were examined. Acquisitions were made with the following motions:

- Continuous motion and a circular orbit (25.5 cm radius Symbia T16 and 30.4 cm radius Discovery NM/CT 670)
- Step and shoot motion and a circular orbit
- Step and shoot motion and a non-circular orbit.

The chosen radii for the circular orbit were the closest possible values of both systems. The other acquisition settings were identical to those described in 3.4.

3.5 Recovery coefficients

The effect of spill-in and spill-out was examined by scanning of the NEMA IEC body Phantom [28]. The NEMA IEC body Phantom has six spheres with diameters of 37 mm, 28 mm, 22 mm, 17 mm, 13 mm and 10 mm. The concentrations for the spheres and background were prepared as follows:

- A known activity was injected in 1L of demineralized water (used for the spheres)
- The same activity (approximately) was injected in the empty cylinder (9.7L volume)

This resulted in a sphere to background ratio of approximately 10:1.
The lung insert remained untouched and it was used to examine the effect of spill-in from the background activity. Figure 3.1 shows an example of the NEMA IEC body phantom.

Figure 3.1: Illustration of the NEMA IEC body phantom. The lung insert in the middle left untouched [28]

The phantom was measured on both imaging systems and the images were reconstructed with the settings described in 3.4. Except the time per projection was 15 seconds and a total scan time of 15 minutes.

The Volumes Of Interests (VOI's) were manually drawn on the CT image first and then translated to the SPECT image. Spherical VOI's were drawn on the hot spheres to measure

the effect of spill-out. Cylindrical VOI's were drawn on the lung insert to examine the spill-in effect and in the background.
The emission recovery coefficients (of the mean counts) due to partial volume artefacts for the spheres were calculated with Equation (3).

$$RC = \frac{Mean\ counts\ VOI - Mean\ Counts\ Background}{\left(Mean\ Counts\ background\ x\ \frac{sph}{back}\ ratio\right) - Mean\ Counts\ background} \quad (3)$$

The RC for the Spill-in was defined as the ratio of the mean counts in the ROI to the mean counts in the background. The RC's were also calculated with a script developed by Georg Schramm [29], [30] which calculates the Full Width at Half Maximum (FWHM) and the RV of each sphere automatically. Besides 3 sample of 1 ml from the background and spheres concentration were measured in the well counter.

3.5.1 Effect of number of updates

The influence of the number of updates was examined by making different reconstructions with varying number of updates given in Table 3.4. The pixel size for the Symbia T16 and Discovery NM/CT 670 were 4.8 mm and 4.4 mm respectively.

3.5.2 Effect of pixel size

The effect of pixel size was examined on the recovery coefficients by varying the pixel size from 3mm-9mm. This was the smallest pixel size possible because at lower values the SPECT projections were outside the Field Of View (FOV). The images were reconstructed with varying updated given in Table 3.4.
The other parameters were identical to those described in 3.5.

3.5.3 Influence of amount of activity

The effect of the amount of activity was examined on the recovery coefficients by varying the activity between 20-500 MBq. The Sphere/Background ratio remained 10:1.
The other parameters were identical to those described in 3.5 except the dwell time was 30 sec for the acquisitions with very low activity (<30MBq) to obtain good count statistics.

4 Results Symbia T16 vs Discovery NM/CT 670

This chapter shows the results obtained from the reconstructions made from the vendors own 3D iterative reconstruction algorithms (Siemens Flash3D and GE Evolution for Bone).
The VOI's were drawn with Hermes Hybrid Viewer PDR 2.5A.

4.1 Quantification

This section shows the results for the measurements with the uniform cylindrical phantom.
The calculated S_{vol} values in a large VOI for the Symbia T16 and Discovery NM/CT 670 were 11.59 ± 0.47 cpm/kBq and 6.11 ± 0.26 cpm/kBq respectively for the imaging parameters described in 3.4.
These settings are very close to those used in many clinical SPECT/CT modalities.
The S_{vol} of the Symbia T16 is 1.89 times higher than the Discovery NM/CT 670.

The S_{vol} of the Discovery NM/CT 670 with a 10% scatter window is 7.88 cpm/kBq. This is 28 % higher than the calculated S_{vol} with a 15% scatter window.

4.1.1 Influence of updates

Table 4.1 shows the S_{vol} values and the error for 4-120 updates for both imaging systems and Figure 4.1 shows a plot of the S_{vol} values in function of the number of updates for both imaging systems. The images were acquired and reconstructed with the settings described in 3.4.

Table 4.1: S_{vol} values for 4-120 updates

updates	S_{vol} symbia T16 (cpm/kBq)	Error S_{vol} Symbia T16	S_{vol} Discovery NM/CT 670 (cpm/kBq)	Error S_{vol} Discovery NM/CT 670
4	9.36	3.65%	2.90	3.90%
8	11.65	3.69%	5.89	4.02%
16	11.76	3.83%	6.26	4.24%
32	11.56	4.05%	6.18	4.51%
64	11.55	4.40%	6.18	4.97%
120	11.59	4.78%	6.18	5.56%

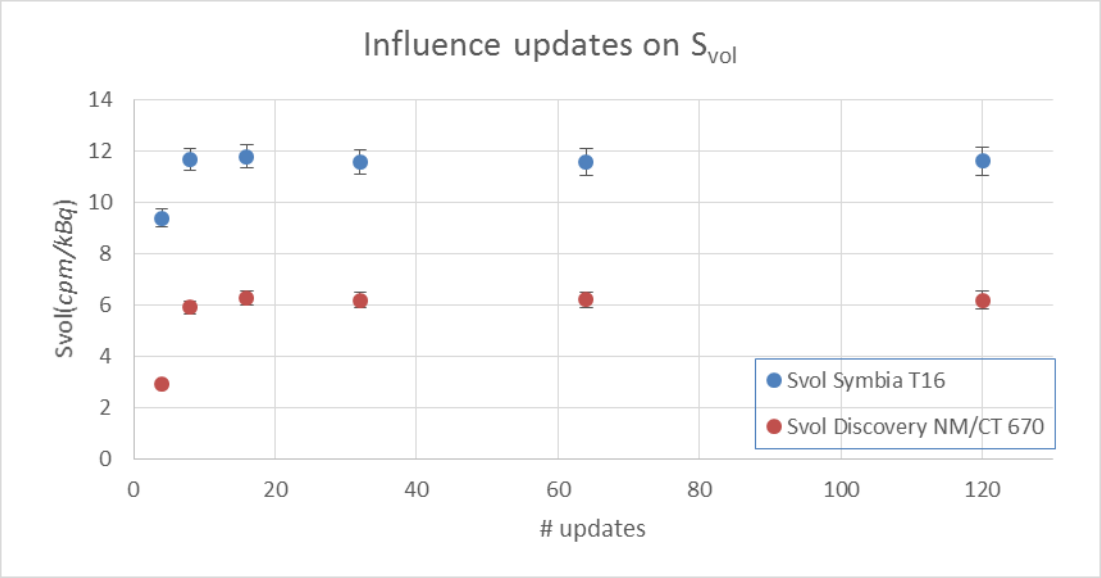

Figure 4.1: S_{vol} values for 4-120 updates Symbia T16 vs Discovery NM/CT 670

The S_{vol} of both imaging systems shows the same pattern. It increases to a maximum value at 16 updates and it stabilises at 32 updates.
The S_{vol} of the Symbia T16 varies from 9.36 cpm/kBq at 4 updates to 11.59 cpm/kBq at 120 updates. It reaches a maximum value of 11.76 cpm/kBq at 16 updates. The error increases from 3.65 % at 4 updates to 4.78% at 120 updates.
The S_{vol} of the Discovery NM/CT 670 varies from 2.90 cpm/kBq at 4 updates to 6.18 cpm/kBq at 120 updates. It reaches a maximum value of 6.26 cpm/kBq at 16 updates. The error increases from 3.90 % at updates to 5.56% at 120 updates.

4.1.2 Influence of pixel size

Table 4.2 shows the S_{vol} values of both imaging systems reconstructed with different pixel sizes. Figure 4.2 shows a plot of the S_{vol} as a function of the pixel size of both imaging systems. The images were acquired and reconstructed with the settings described in 3.4.

Table 4.2: S_{vol} values for different pixel sizes. Left: Symbia T16. Right: Discovery NM/CT 670

Pixelsize (mm)	S_{vol} (cpm/kBq)	% error
2.40	11.33	4.27%
4.80	11.59	4.77%
9.59	11.63	5.67%

Pixelsize (mm)	S_{vol} (cpm/kBq)	% error
2.21	5.79	5.05%
4.42	6.18	5.56%
8.83	5.93	4.57%

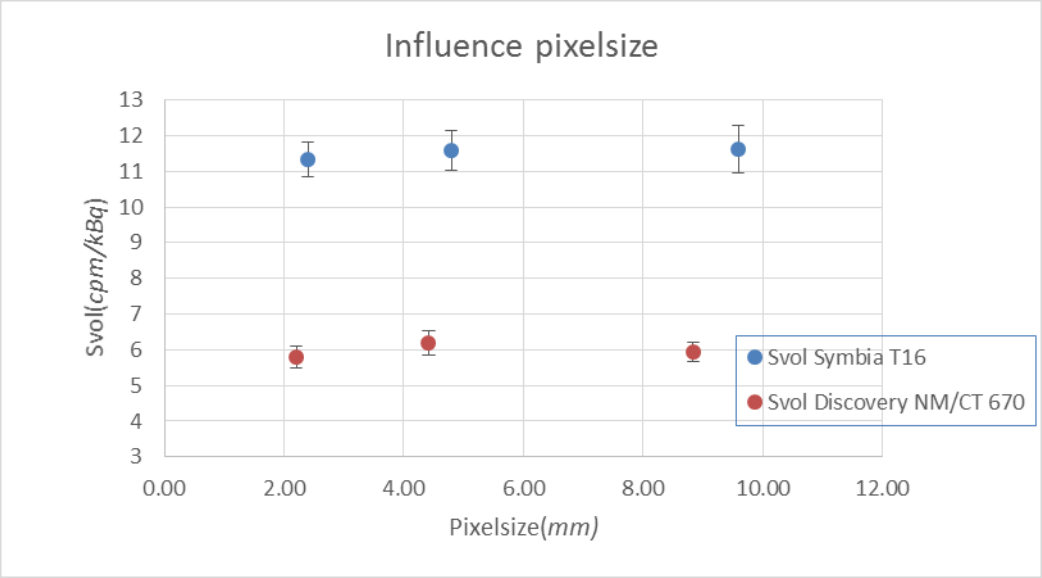

Figure 4.2: S_{vol} values for different pixel sizes

The S_{vol} of the Symbia T16 increases from 11.33 cpm/kBq (2.40 mm pixels) to 11.63 cpm/kBq (9.59 mm pixels). This is an increase of 2 %. Considering the error on the S_{vol} is approximately 5 % this variation is negligible. The error on the S_{vol} increases from 4.27% (2.4 mm pixels) to 5.67% (9.59 mm pixels). The error increases with larger pixel size.

The S_{vol} of the Discovery NM/CT 670 varies from 5.79 cpm/kBq (2.21 mm pixels) to 5.93 cpm/kBq (8.83 mm pixels). The S_{vol} reaches a maximum at 4.42 mm pixels with 6.18 cpm/kBq.
The error on the S_{vol} varies between 4.57% (8.83 mm pixels) and 5.56% (4.42 mm pixels). The error increases with decreasing pixel size. However, the error with 2.21 mm pixels is higher than the error of 4.42 mm pixels.

4.1.3 Influence of activity

Table 4.3 shows the S_{vol} values of both imaging systems reconstructed with different activities. Figure 4.3 shows a plot of the S_{vol} as a function of the activity during acquisition of both imaging systems. The images were acquired and reconstructed with the settings described in 3.4.

Table 4.3: S_{vol} values at activities 0-500 MBq. Left: Symbia T16. Right: Discovery NM/CT 670

Act at start acq. (MBq)	S_{vol} (cpm/kBq)	% error
23.33	11.93	7.18%
203.87	11.66	6.40%
345.87	11.51	5.24%
465.71	11.47	4.66%
470.86	11.59	4.77%
545.69	11.59	4.05%

Act at start acq. (MBq)	S_{vol} (cpm/kBq)	% error
25.73	6.93	7.02%
230.10	6.38	6.44%
329.24	6.20	5.47%
412.42	6.18	4.72%
413.43	6.06	5.66%
500.51	6.11	4.31%

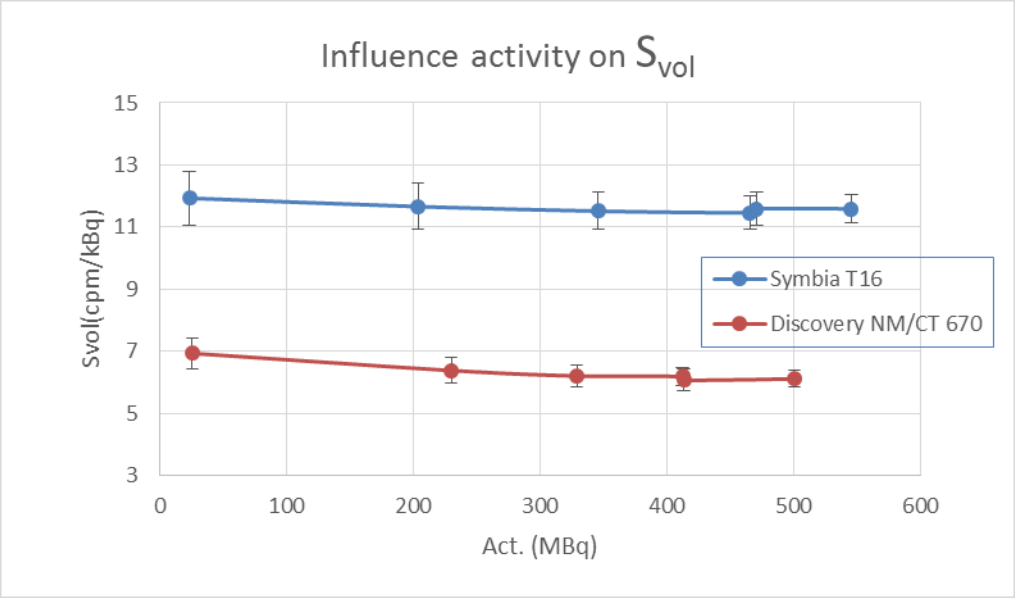

Figure 4.3: S_{vol} values for activities 0-500 MBq

The S_{vol} of both imaging systems shows a similar pattern. The S_{vol} decreases with increasing activity and stabilises around 400-500 MBq. The error decreases with increasing activity.
The S_{vol} of the Symbia T16 varies betwees 11.47-11.93 cpm/kBq. Considering of the error on the S_{vol} of approximately 5% this variation is negligible.
The error on the S_{vol} decreases from 7.18% to 4.05% with increasing activity.
The S_{vol} of the Discovery NM/CT 670 varies between 6.06-6.93 cpm/kBq (This is a fluctuation of 14%). The error on the S_{vol} decreases from 7.02% to 4.31% with increasing activity.

4.1.4 Influence of detector motion and orbit

Table 4.4 shows the S_{vol} values for different detector motion and orbit of both imaging systems. The images were acquired and reconstructed with the settings described in 3.4.
There is no measurement with a continuous detector motion and a non-circular detector orbit for the Discovery NM/CT 670 because the operating software does not allow it.

Table 4.4: S_{vol} values for different detector settings of both imaging systems

		Symbia T16		Discovery NM/CT 670	
Detector motion	**Detector orbit**	**S_{vol} (cpm/kBq)**	**error S_{vol}**	**S_{vol} (cpm/kBq)**	**error S_{vol}**
Continuous	Circular	11.41	4.27%	5.91	4.54%
Continuous	Non circular	11.59	4.05%	/	/
Step and shoot	Circular	11.62	4.61%	5.97	4.61%
Step and shoot	Non circular	11.70	4.67%	6.11	4.31%

On the Symbia T16, the S_{vol} varies between 11.41-11.70 cpm/kBq.
On the Discovery NM/CT 670, the S_{vol} varies between 5.91-6.11 cpm/kBq. Considering the error on the S_{vol} is approximately 5%, the variations are negligible for both systems.

4.1.5 Uniformity analysis

This section gives the results of the uniformity analysis for the measurements made with the uniform cylindrical phantom. Figure 4.4 shows the uniformity and standard deviation analysis of both imaging systems for the imaging settings described in 3.4. The dashed purple lines show the inner 80 % of the phantom. The x-axis shows the slice number of the SPECT image. The y-axis on the uniformity graphs shows the calculated activity concentration. This was calculated by dividing the mean count density in each ROI with the calculated S_{vol}. The error bars show the standard deviation on the mean activity concentration of each slice. The standard deviation graphs show the % standard deviation and the % deviation to the mean activity in each slice.

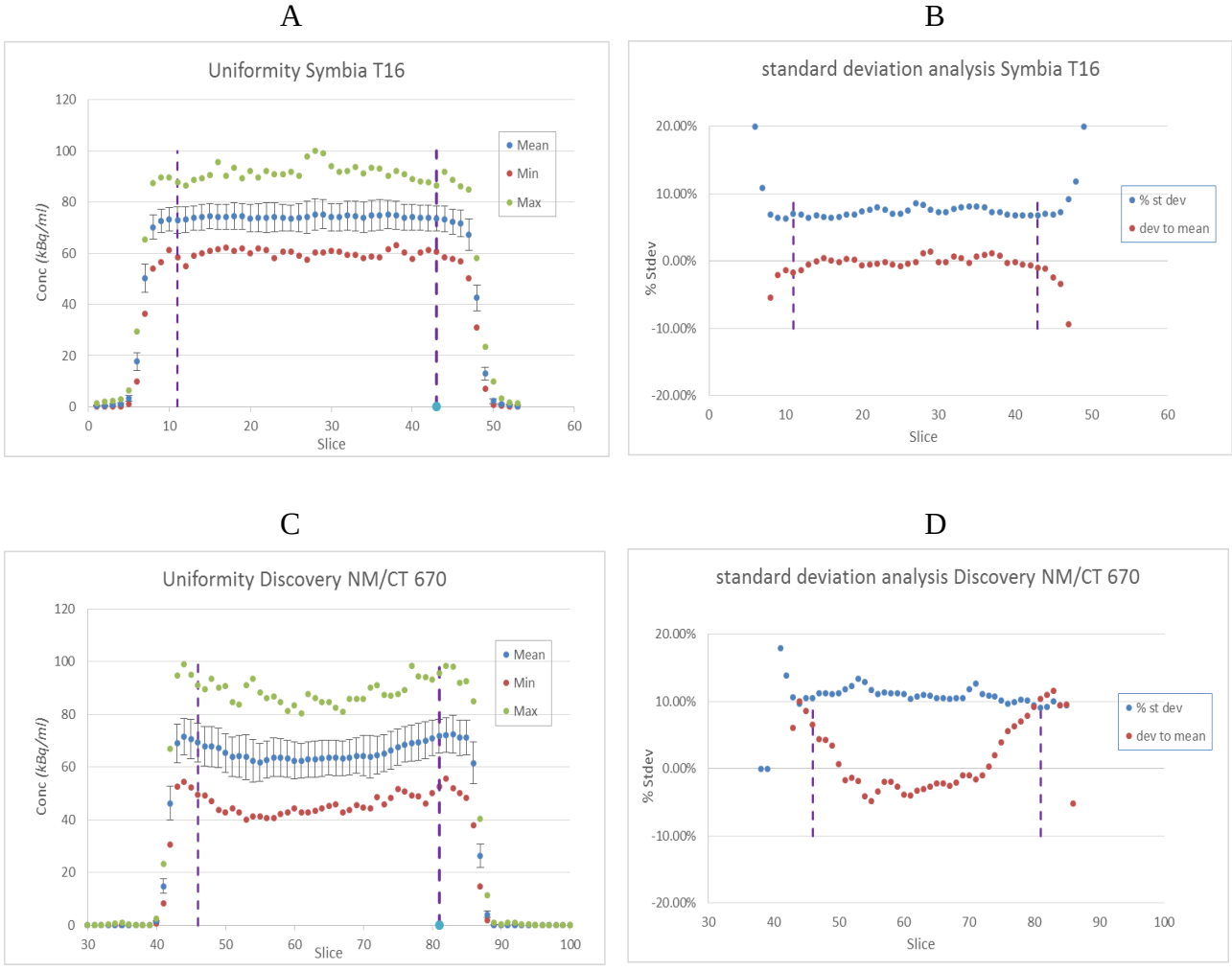

Figure 4.4: Uniformity and standard deviation analysis of both imaging systems. (A,B): uniformity and standard deviation analysis Symbia T16. (C,D): Uniformity and standard deviation analysis Discovery NM/CT 670

The activity concentration stays uniform for the Symbia T16. There is a cupping pattern visible in the middle of the phantom for the Discovery NM/CT 670. It shows signs of under correction for photon attenuation.

Figure 4.5 shows the uniformity analysis and Figure 4.6 shows the standard deviation analysis for 4, 32, 120 updates of both imaging systems. The dashed purple lines represent the inner 80% of the phantom.

4 updates

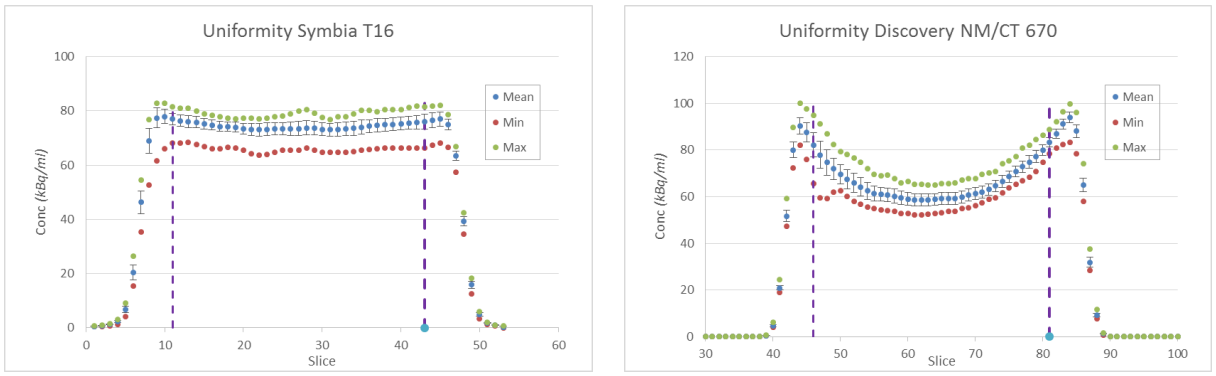

32 updates

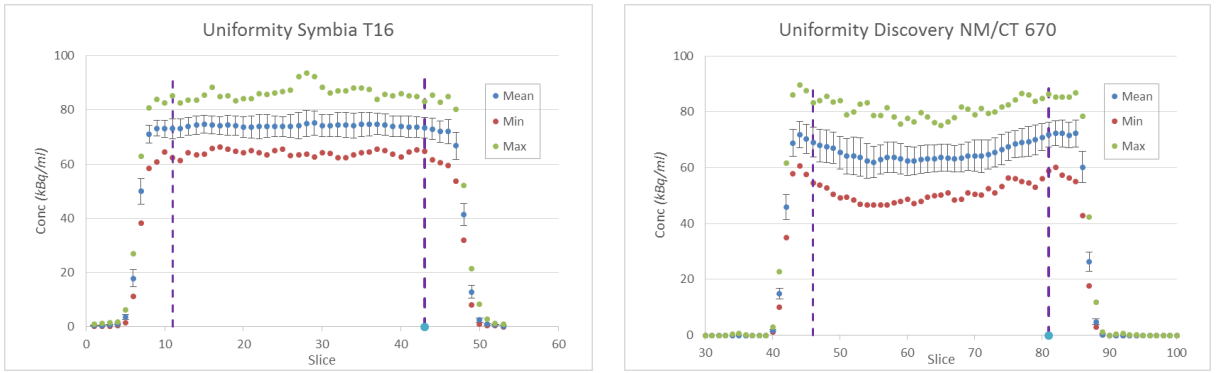

120 updates

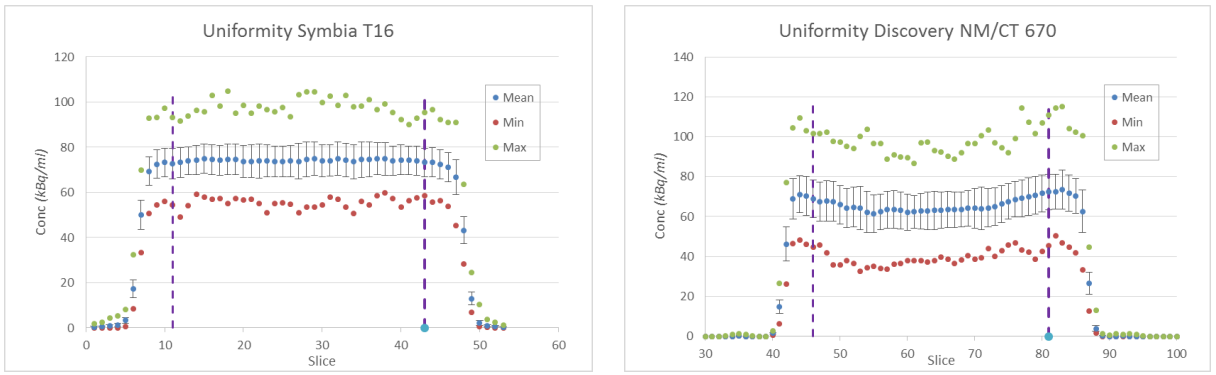

Figure 4.5: Uniformity analysis of both imaging systems at 4,32,120 updates. Left: Symbia T16. Right: Discovery NM/CT 670

4 updates

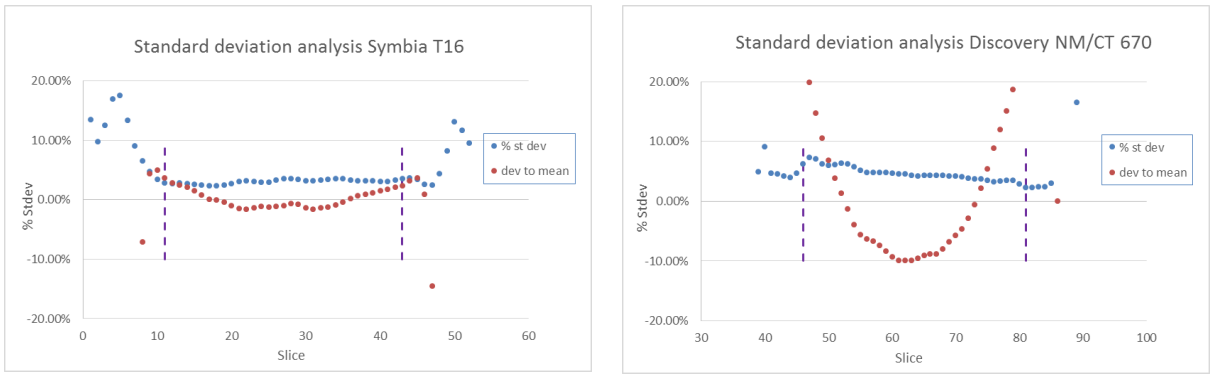

32 updates

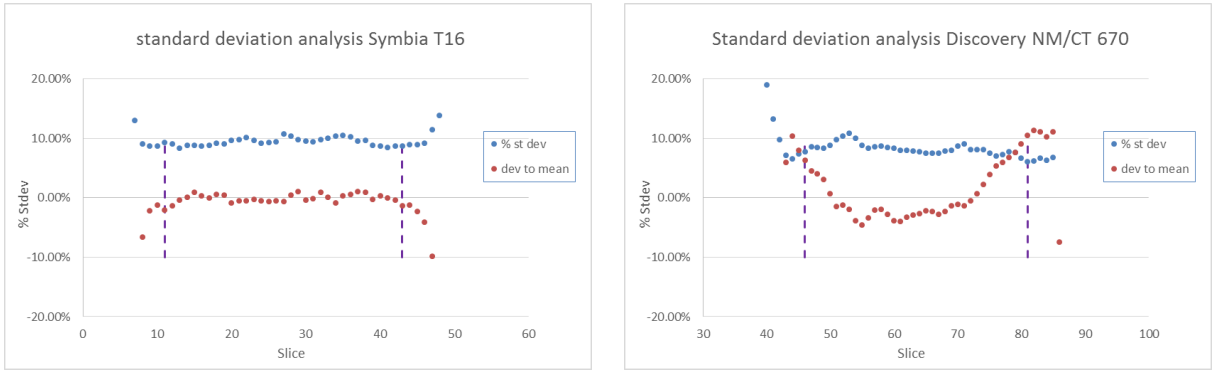

120 updates

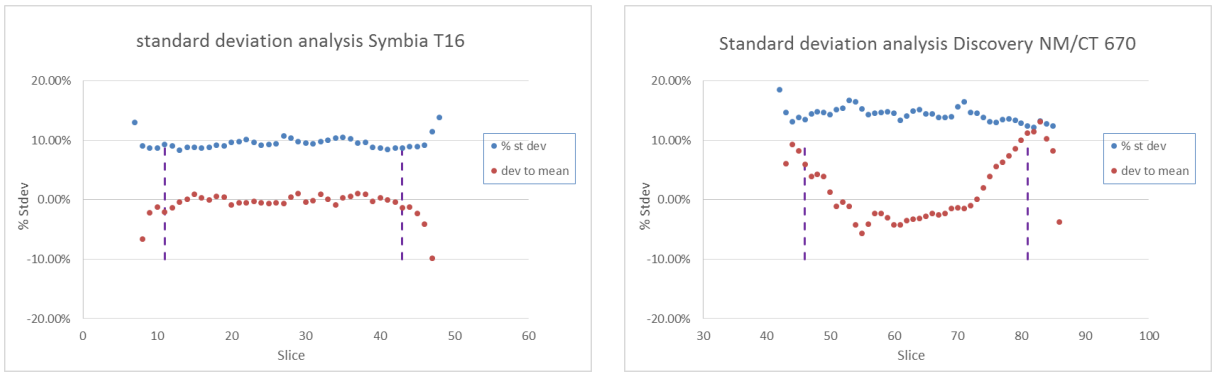

Figure 4.6 : Standard deviation analysis of both imaging systems at 4,32,120 updates. Left: Symbia T16. Right: Discovery NM/CT 670

The uniformity stays constant for the Symbia T16. At 4 updates, a large cupping artefact in the middle of the phantom is visible for the Discovery NM/CT 670. This effect lessens at more updates.

Figure 4.7 shows the uniformity analysis and Figure 4.8 shows the standard deviation analysis for different pixel sizes of both imaging systems. The dashed purple lines represent the inner 80% of the phantom.

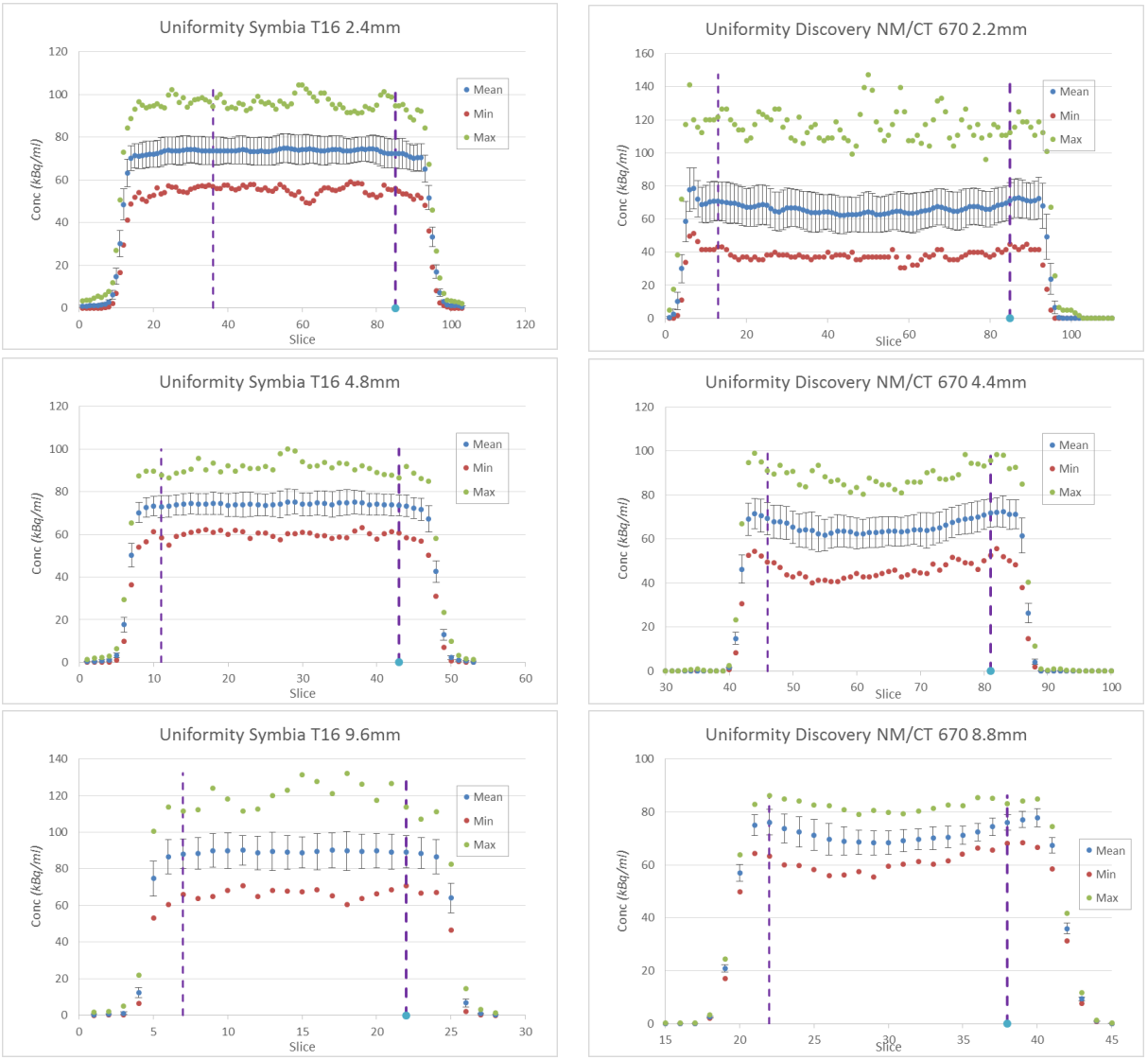

Figure 4.7: Uniformity analysis of both imaging systems at different pixel sizes. Left: Symbia T16. Right: Discovery NM/CT 670

Figure 4.8: Standard deviation analysis of both imaging systems at different pixel sizes. Left: Symbia T16. Right: Discovery NM/CT 670

The activity remains uniform for the Symbia T16. However, small oscillation artefacts are visible at 2.4 mm and 4.8 mm pixels.
There is a cupping artefact visible in the middle of the phantom for the Discovery NM/CT 670. At 2.2 mm and 4.4 mm pixels, oscillation artefacts are visible (predominant at 2.2 mm pixels).

4.2 Emission recovery coefficients

This section shows the results for the measurements with the NEMA IEC body phantom [28]. The images were reconstructed with the vendors own reconstruction algorithms. The VOI's were drawn with Hermes Hybrid Viewer PDR 2.5A.
Figure 4.9 shows the emission recovery values for different sphere sizes for 3.3 mm, 4.8mm and 9.6 mm^3 pixels with varying updates from 4 to 120 for the Siemens Symbia T16.

[3] There are no Recovery Values for the smallest sphere (10mm diameter) with 9.6mm pixels for the Symbia T16 because the VOI was not translated correctly from the CT image to the SPECT image.

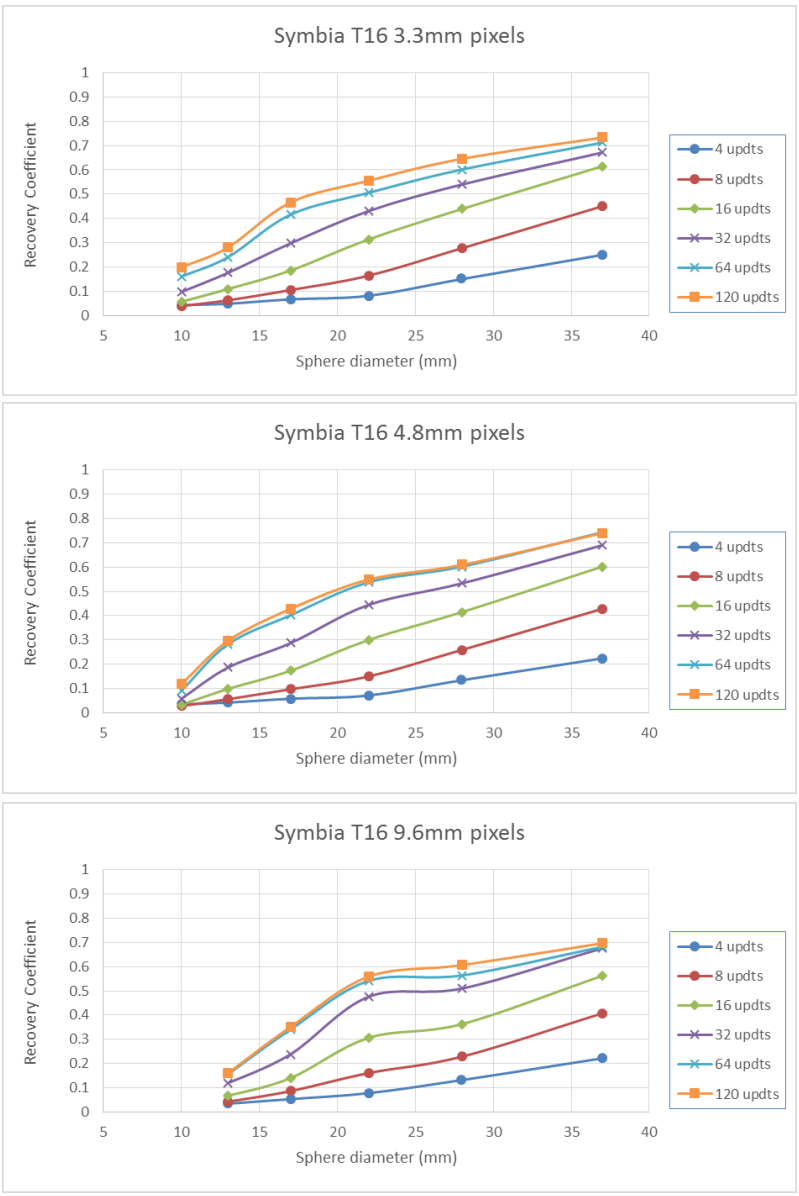

Figure 4.9: Recovery values for different object sizes for 3.3mm, 4.8mm and 9.6mm pixels with varying updates for Siemens Symbia T16

At 3.3 mm pixels, the recovery value (RV) of the biggest sphere is 0.71 at 64 updates and 0.73 at 120 updates. For the smallest sphere, the RV drops to 0.16 at 64 updates and 0.19 at 120 updates. The recovery values seem so stabilize at 64 updates. At 4 updates, the RV of the smallest sphere drops below 0.045 and for the biggest sphere it reaches a value of 0.25.
At 4.8 mm pixels, the pattern is similar except that the RV's for the smaller spheres are twice as low than at 3.3 mm pixels. The RV is 0.74 for the biggest sphere and 0.09 for the smallest. At 4 updates, the RV of the smallest sphere drops below 0.035 and for the biggest sphere the RV is 0.22.
At 9.6 mm pixels, the RV's of the smallest spheres drop again approximately by a factor 2 compared to 4.8 mm pixels. At 64 updates, the RV is 0.69 for the biggest sphere.

Figure 4.10 shows the emission recovery values for different sphere sizes for 2.9 mm, 4.4 mm and 8.8 mm pixels with varying updates from 4 to 120 for GE Discovery NM/CT 670.

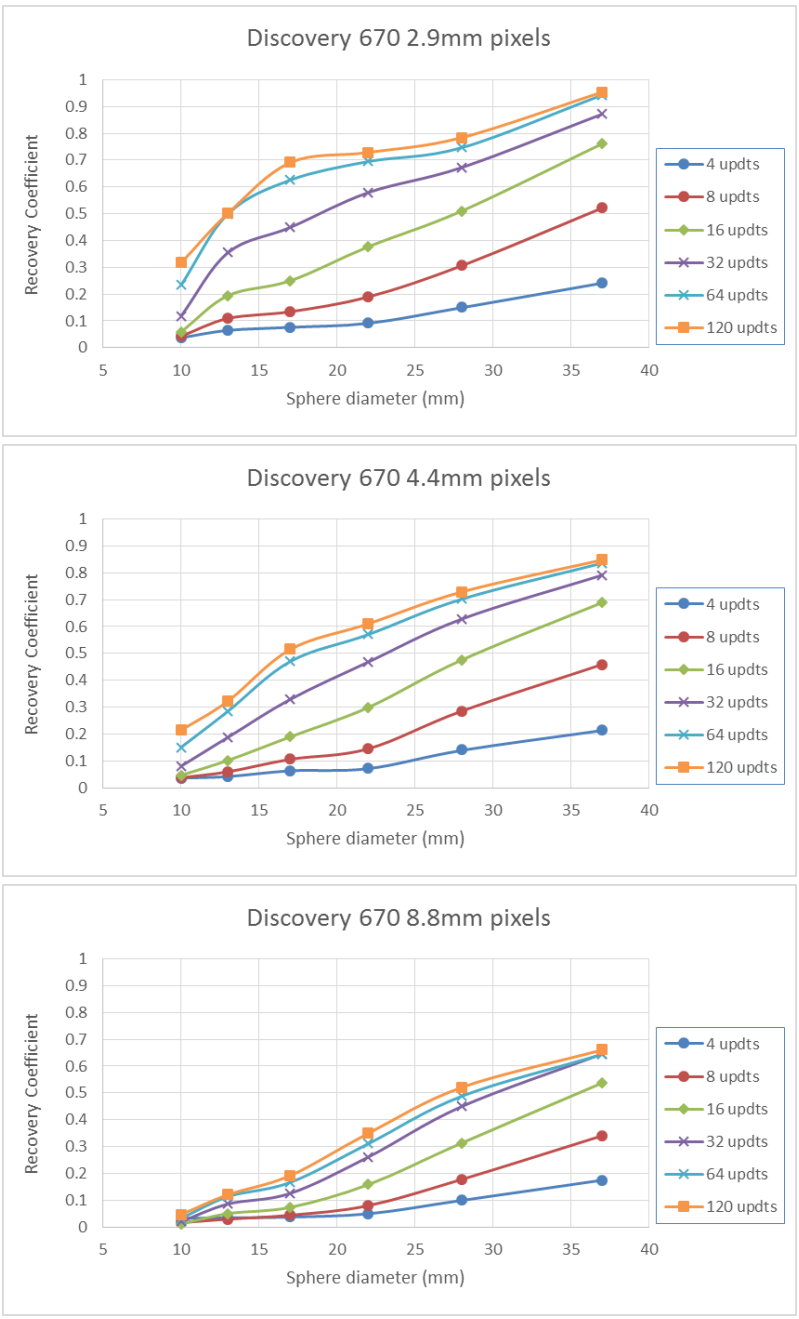

Figure 4.10: Recovery values for different object sizes for 2.9mm, 4.4mm and 8.8mm pixels with varying updates for GE Discovery NM/CT 670

The RV's are approximately 10% higher than for Siemens Symbia T16.
At 2.9 mm pixels, the recovery value (RV) of the biggest sphere is 0.94 at 64 updates and 0.95 at 120 updates. For the smallest sphere, the RV drops to 0.23 at 64 updates and 0.31 at 120 updates. The recovery values seem so stabilize at 64 updates. At 4 updates, the RV of the smallest sphere drops below 4% and for the biggest sphere it reaches a value of 0.24.
At 4.4 mm pixels, the pattern is similar except that the RV's are approximately 15% lower than at 3.3 mm pixels. The RV is 0.83 for the biggest sphere and 0.21 for the smallest. At 4 updates, the RV of the smallest sphere is 0.036 and for the biggest sphere the RV is 0.21.
At 8.83 mm pixels, the RV's of the bigger spheres drop with approximately 20%. At 64 updates, the RV is 0.64 for the biggest sphere.

4.2.1 Influence of activity

Figure 4.11 shows the Recovery Values (RV) for the different spheres at different activities.

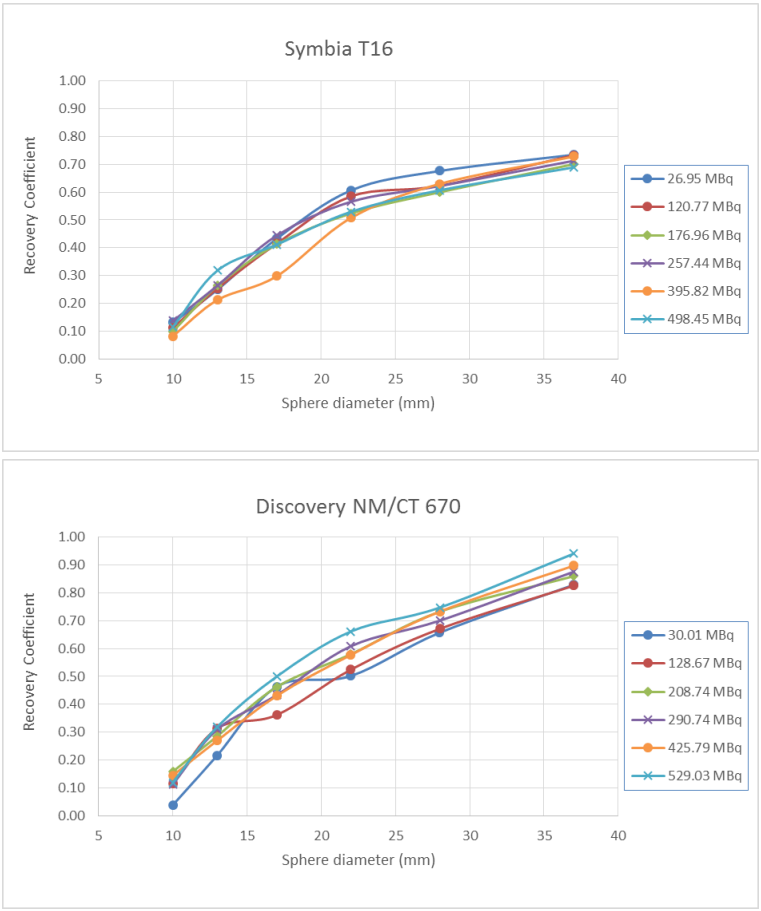

Figure 4.11: Recovery values in function of the sphere diameter at different activities.

For the Symbia T16, the recovery values for the spheres do not vary significantly at different activities. For the Discovery NM/CT 670, the RV's of the smaller spheres is 3 times less at very low activities (± 30 MBq). For the bigger spheres, the RV's increase with 10% at higher activities.

4.2.2 Effect of spill-in

Table 4.5 shows the RV's of the lung insert (to measure the effect of spill-in) at different pixel sizes and varying updates and Figure 4.12 shows the RV's for the lung insert as a function of the pixel size for both imaging systems.

Table 4.5: Recovery values for the spill-in effect for different pixel sizes and varying updates of both imaging systems.

Siemens Symbia T16

	Recovery values Spill-in					
Pixel size (mm)	**4updts**	**8updts**	**16updts**	**32updts**	**64updts**	**120updts**
3.3	0.86	0.92	0.70	0.38	0.24	0.27
4.8	0.85	0.71	0.56	0.39	0.24	0.17
9.6	1.07	0.95	0.53	0.51	0.22	0.15

GE Discovery NM/CT 670

	Recovery values Spill-in					
Pixel size (mm)	**4updts**	**8updts**	**16updts**	**32updts**	**64updts**	**120updts**
2.9	0.74	0.63	0.65	0.40	0.14	0.14
4.8	0.80	0.91	0.61	0.26	0.20	0.08
9.6	1.13	0.92	0.69	0.35	0.29	0.20

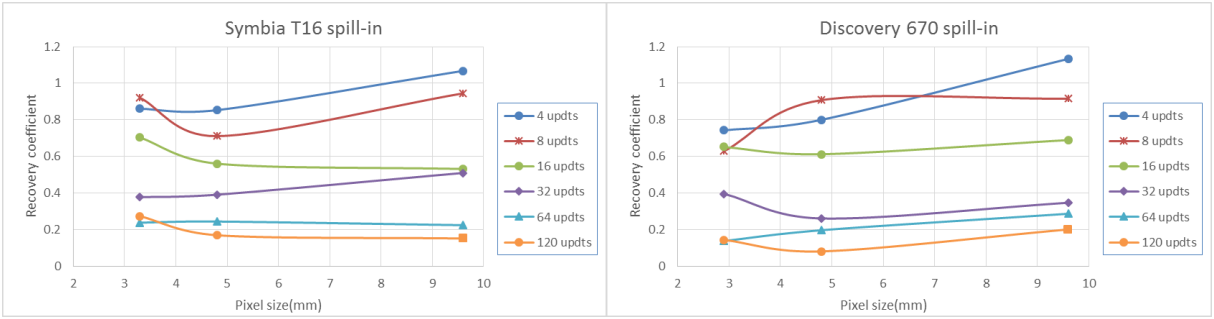

Figure 4.12: Effect of spill-in for different pixel sizes at varying updates from 4-120. Left: Siemens Symbia T16. Right: GE Discovery NM/CT 670

The RV's drop with decreasing pixel size and increasing updates but it stabilizes at 64 updates. At 4 updates and large pixel sizes, the RV increases above 100%. At 64 updates, the RV's are similar for different pixel sizes. At 120 updates, the RV's are still about 0.15.

5 Results Hybridrecon

This chapter shows the results obtained from the reconstructions made with Hermes Hybridrecon.
The VOI's were drawn with Hermes Hybrid Viewer PDR 2.5A.

5.1 Quantification

The calculated System Volume Sensitivity (S_{vol}) in a large VOI for the Symbia T16 and Discovery NM/CT 670 were 8.93 ± 0.44 cpm/kBq and 6.70 ± 0.27 cpm/kBq respectively for the imaging parameters described in 3.4.
The S_{vol} of the Symbia T16 is 1.3 times higher than the Discovery NM/CT 670.

The calculated S_{vol} values from the reconstructions with Hybridrecon vary significantly from the S_{vol} values from the reconstructions with the vendors algorithms (Flash3D and GE Evolution for Bone).
For the Symbia T16, the S_{vol} value with the Hybridrecon is 23% lower than the Svol value with Flash3D.
For the Discovery NM/CT 670, the S_{vol} value with the Hybridrecon is 9.6% higher than the Svol value with Flash3D.

5.1.1 Influence of updates

Table 5.1 shows the S_{vol} values and the error for 4-120 updates for both imaging systems and Figure 5.1 shows a plot of the S_{vol} values in function of the number of updates for both imaging systems. The images were acquired and reconstructed with the settings described in 3.4 (with Hermes Hybridrecon Oncology algorithm).

Table 5.1: S_{vol} values for 4-120 updates (Reconstructed with Hermes Hybridrecon)

Updates	S_{vol} symbia T16(cpm/kBq)	Error S_{vol} Symbia T16	S_{vol} Discovery NM/CT 670 (cpm/kBq)	Error S_{vol} Discovery NM/CT 670
4	9.14	4.39%	7.04	4.21%
8	9.74	3.78%	7.47	3.59%
16	9.05	3.81%	6.95	3.81%
32	8.84	4.04%	6.82	4.06%
64	8.89	4.43%	6.88	4.42%
120	8.93	4.95%	6.94	4.89%

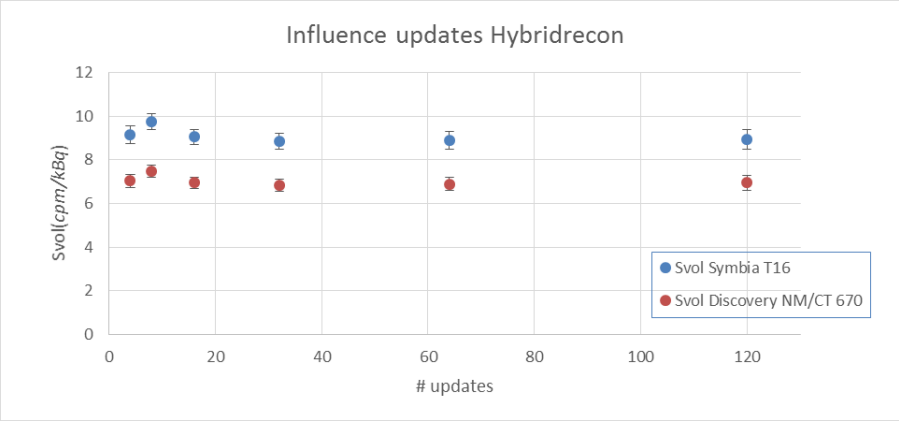

Figure 5.1: S_{vol} values for 4-120 updates Symbia T16 vs Discovery NM/CT 670 (Reconstructed with Hermes Hybridrecon)

The S_{vol} of both imaging systems show the same pattern. It increases to a maximum value at 8 updates and it stabilises at 32 updates.
The S_{vol} of the Symbia T16 varies from 9.14 cpm/kBq at 4 updates to 8.93 cpm/kBq at 120 updates. It reaches a maximum value of 9.74 cpm/kBq at 8 updates. The error increases from 4.93 % at 4 updates to 4.95% at 120 updates.
The S_{vol} of the Discovery NM/CT 670 varies from 7.04 cpm/kBq at 4 updates to 6.94 cpm/kBq at 120 updates. It reaches a maximum value of 7.47 cpm/kBq at 8 updates. The error increases from 3.59 % at 8 updates (except the error at 4 updates is higher) to 4.89% at 120 updates.

5.1.2 Influence of pixel size

Table 5.2 shows the S_{vol} values of both imaging systems reconstructed with different pixel sizes. Figure 5.2 shows a plot of the S_{vol} as a function of the pixel size of both imaging systems. The images were acquired and reconstructed with the settings described in 3.4 (with Hermes Hybridrecon Oncology algorithm).

Table 5.2: S_{vol} values for different pixel sizes. Left: Symbia T16. Right: Discovery NM/CT 670 (Reconstructed with Hermes Hybridrecon)

Pixelsize (mm)	S_{vol} (cpm/kBq)	% error
2.40	8.66	4.35%
4.80	8.93	4.95%
9.59	8.95	5.65%

Pixelsize (mm)	S_{vol} (cpm/kBq)	% error
2.21	6.34	4.12%
4.42	6.94	4.89%
8.83	6.65	5.18%

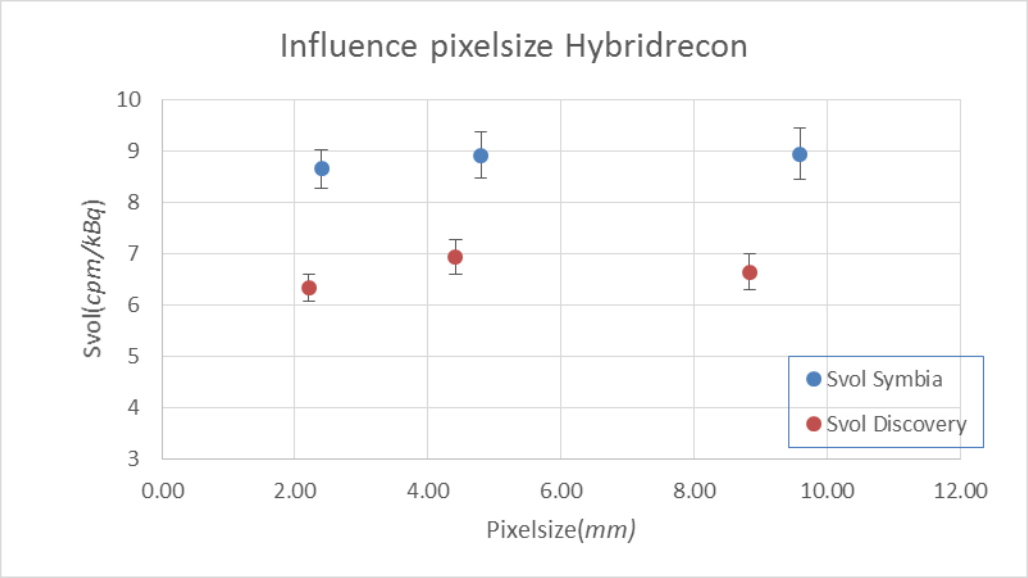

Figure 5.2: S_{vol} values for different pixel sizes (Reconstructed with Hermes Hybridrecon)

The S_{vol} of the Symbia T16 increases from 8.66 cpm/kBq (2.4 mm pixels) to 8.95 cpm/kBq (9.59 mm pixels). Considering the error on the S_{vol} is approximately 5 % this increase is negligible. The error on the S_{vol} increases from 4.35% (2.4 mm pixels) to 5.65 % (9.59 mm pixels). The error increases with larger pixel size.

The S_{vol} of the Discovery NM/CT 670 varies from 6.34 cpm/kBq (2.21 mm pixels) to 6.65 cpm/kBq (8.83 mm pixels). It reaches a maximum value of 6.94 cpm/kBq with 4.42 mm pixels.
The error on the S_{vol} increases from 4.12% (2.21 mm pixels) to 5.18 % (8.83 mm pixels). The error increases with larger pixels.

5.1.3 Influence of activity

Table 5.3 shows the S_{vol} values of both imaging systems reconstructed with different activities. Figure 5.3 shows a plot of the S_{vol} as a function of the activity during acquisition of both imaging systems. The images were acquired and reconstructed with the settings described in 3.4.

Table 5.3: S_{vol} values at activities 0-500 MBq. Left: Symbia T16. Right: Discovery NM/CT 670 (Reconstructed with Hermes Hybridrecon)

Act at start acq. (MBq)	S_{vol} (cpm/kBq)	% error
23.33	9.04	7.38%
203.87	8.98	6.48%
345.87	8.84	5.43%
465.71	8.81	4.69%
470.86	8.93	4.95%

Act @ start acq. (MBq)	S_{vol} (cpm/kBq)	% error
25.73	7.36	6.17%
230.10	7.00	5.80%
329.24	6.84	4.91%
412.42	6.94	4.32%
413.43	6.77	5.01%
500.51	6.70	3.98%

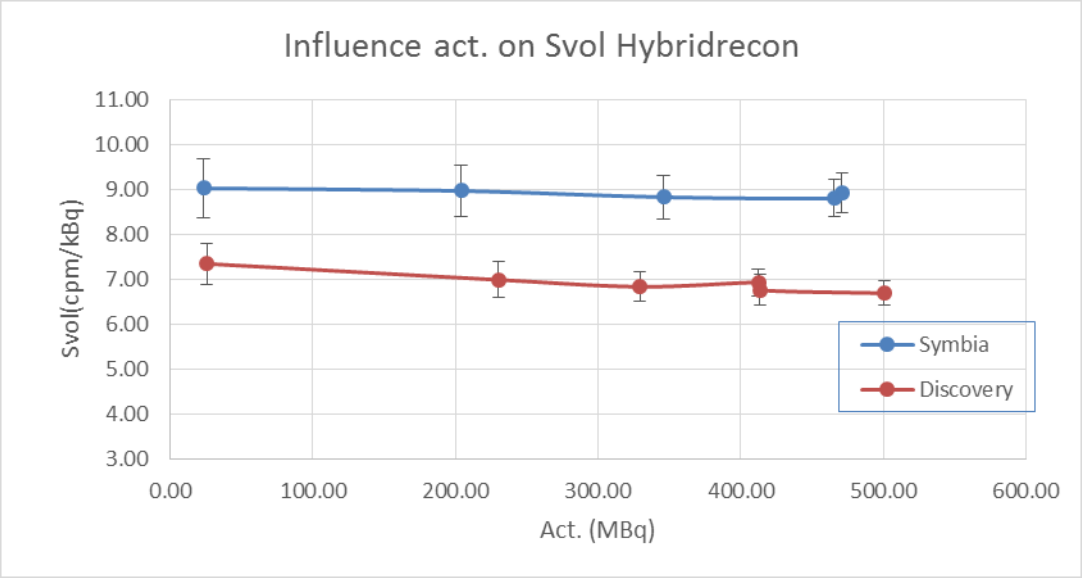

Figure 5.3: S_{vol} values for activities 20-500 MBq (Reconstructed with Hermes Hybridrecon)

The S_{vol} of both imaging systems show a similar pattern. The S_{vol} decreases with increasing activity and it stabilises around 400-500 MBq. The error decreases with increasing activity.
The S_{vol} of the Symbia T16 varies betwees 8.81-9.04 cpm/kBq. Considering the error on the Svol of approximately 5% this variation is negligible.
The error on the S_{vol} decreases from 7.38% to 4.95% with increasing activity.
The S_{vol} of the Discovery NM/CT 670 varies between 6.77-7.36 cpm/kBq. The error on the S_{vol} decreases from 6.17% to 3.98% with increasing activity.

5.1.4 Influence of detector motion and orbit

Table 4.4 shows the S_{vol} values for different detector motion and orbit of both imaging systems. The images were acquired and reconstructed with the settings described in 3.4 (reconstructed with Hermes Hybridrecon).
There is no measurement with a continuous detector motion and a non-circular detector orbit for the Discovery NM/CT 670 because the operating software does not allow it.

Table 5.4: S_{vol} values for different detector settings of both imaging systems (reconstructed with Hermes Hybridrecon)

		Symbia T16		Discovery NM/CT 670	
Detector motion	**Detector orbit**	**S_{vol} (cpm/kBq)**	**error S_{vol}**	**S_{vol} (cpm/kBq)**	**error S_{vol}**
Continuous	Circular	8.69	4.23%	6.57	4.15%
Continuous	Non circular	8.93	4.95%	/	/
Step and shoot	Circular	8.95	4.60%	6.49	4.43%
Step and shoot	Non circular	9.03	4.62%	6.70	3.98%

On the Symbia T16, the Svol varies between 8.69-9.03 cpm/kBq.
On the Discovery NM/CT 670, the S_{vol} varies between 6.49-6.70 cpm/kBq. Considering the error on the S_{vol} is approximately 4% these variations are negligible for both systems.

5.1.5 Uniformity analysis

This section gives the results for the uniformity analysis for the measurements made with the uniform cylindrical phantom. Figure 5.4 shows the uniformity and standard deviation analysis of both imaging systems for the imaging settings described in 3.4 (reconstructed with Hermes Hybridrecon). The dashed purple lines show the inner 80 % of the phantom. The x-axis shows the slice number of the SPECT image. The y-axis on the uniformity graphs shows the calculated activity concentration. This was calculated by dividing the mean count density in each ROI with the calculated S_{vol}.

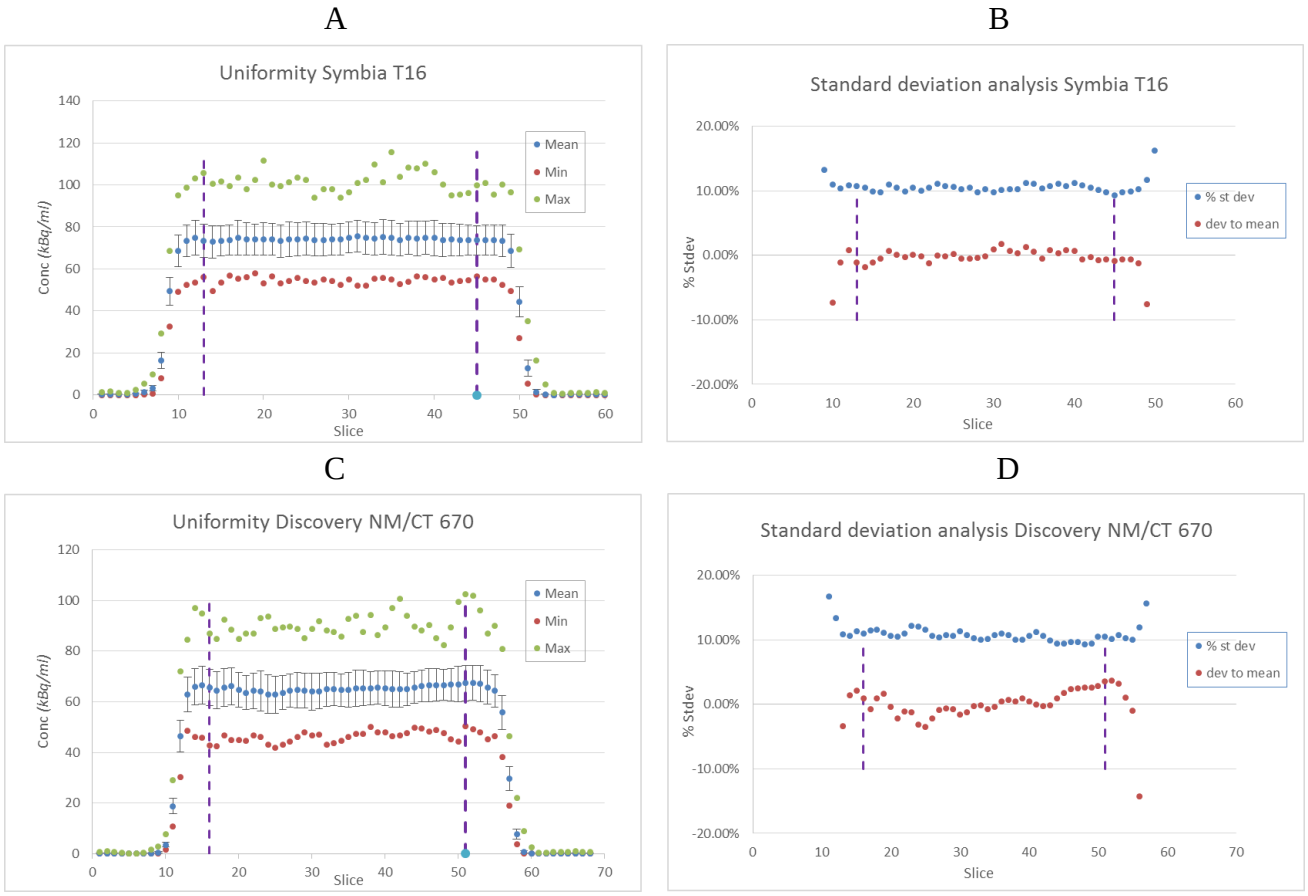

Figure 5.4: Uniformity and standard deviation analysis of both imaging systems. (A,B): uniformity and standard deviation analysis Symbia T16. (C,D): Uniformity and standard deviation analysis Discovery NM/CT 670 (Reconstructed with Hermes Hybridrecon)

The activity concentration stays uniform for the Symbia T16. There are oscillation artefacts visible for the Discovery NM/CT 670.

Figure 5.5 shows the uniformity analysis and Figure 5.6 shows the standard deviation analysis for 4, 32, 120 updates of both imaging systems. The dashed purple lines represent the inner 80% of the phantom.

4 updates

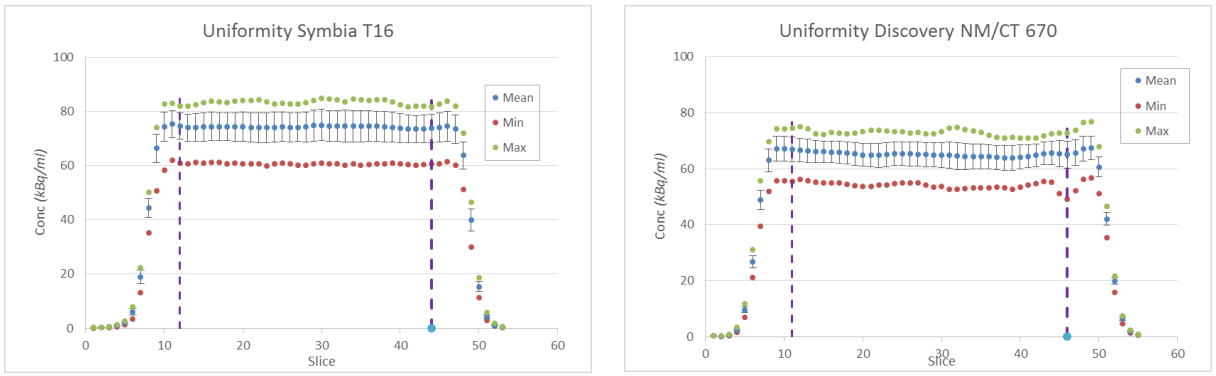

32 updates

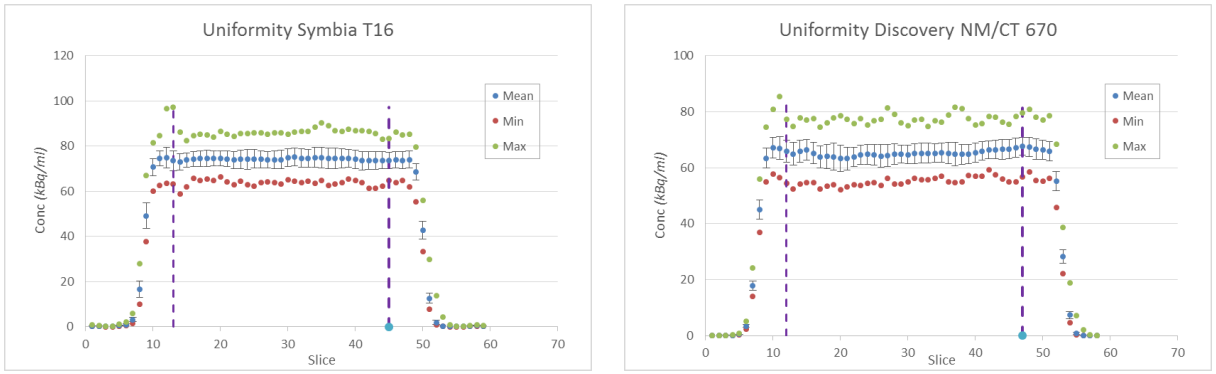

120 updates

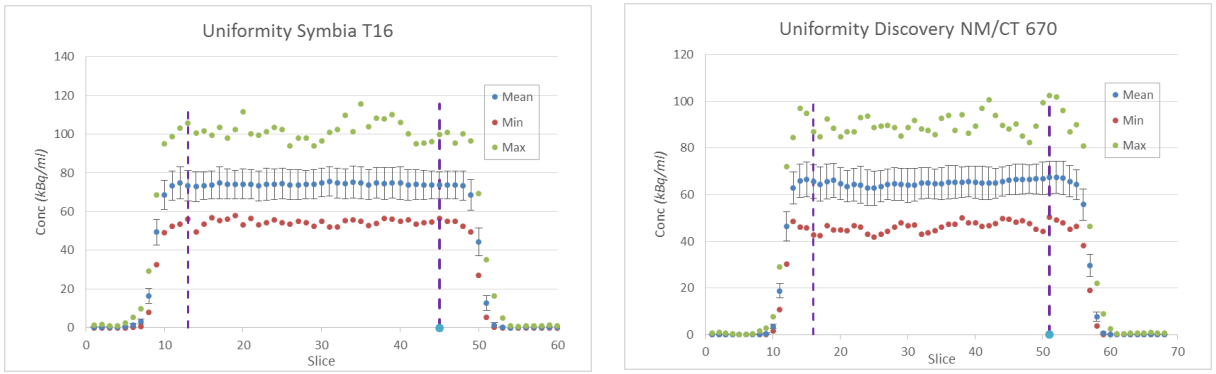

Figure 5.5 : Uniformity analysis of both imaging systems at different pixel sizes. Left: Symbia T16. Right: Discovery NM/CT 670 (reconstructed with Hermes Hybridrecon)

4 updates

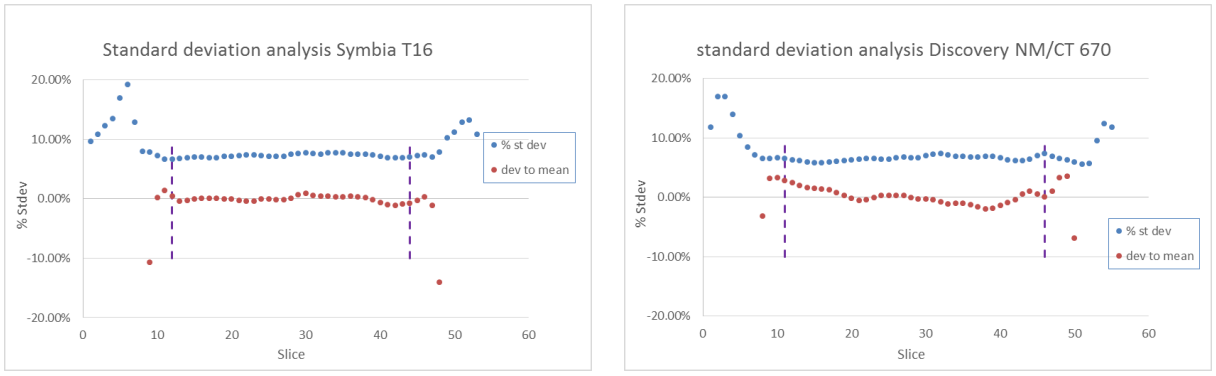

32 updates

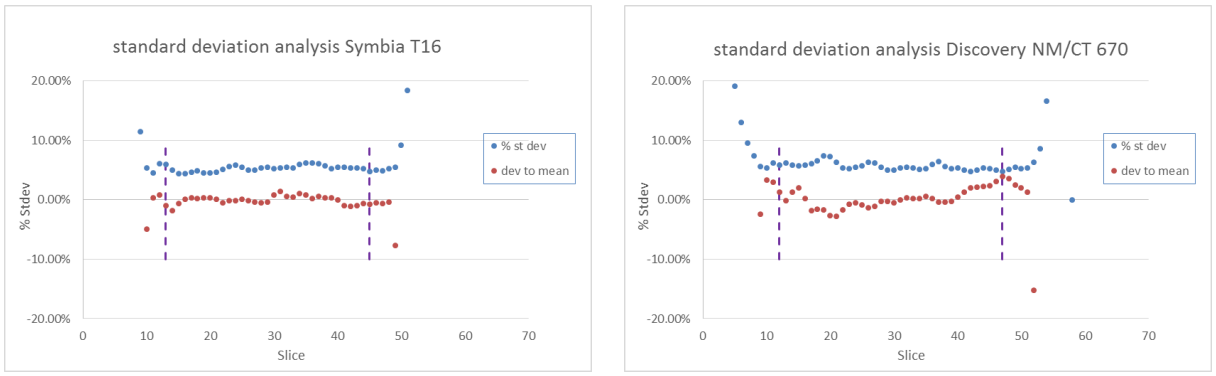

120 updates

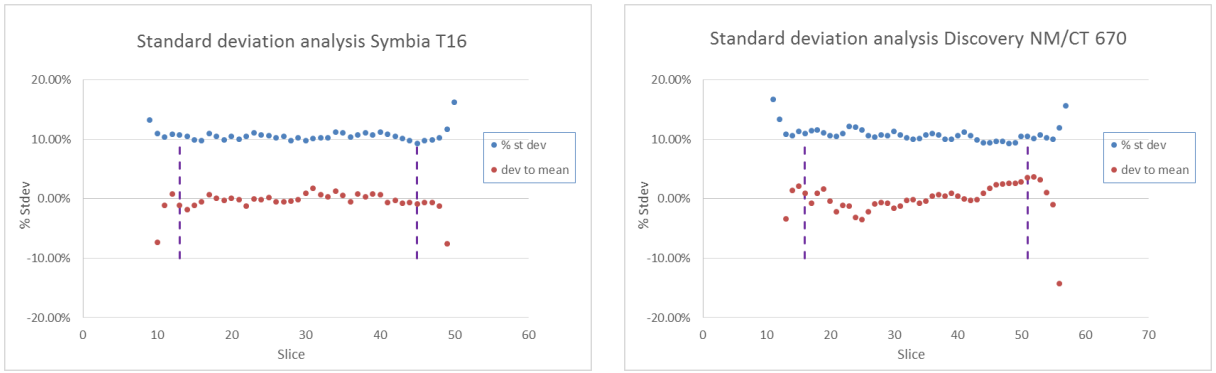

Figure 5.6 : Standard deviation analysis of both imaging systems at different pixel sizes. Left: Symbia T16. Right: Discovery NM/CT 670 (reconstructed with Hermes Hybridrecon)

The activity concentration remains uniform for the Symbia T16. There are oscillation artefacts visible for the Discovery NM/CT 670. These are more apparent at 120 updates.

Figure 4.7 shows the uniformity analysis and Figure 4.8 shows the standard deviation analysis for different pixel sizes of both imaging systems. The dashed purple lines represent the inner 80% of the phantom.

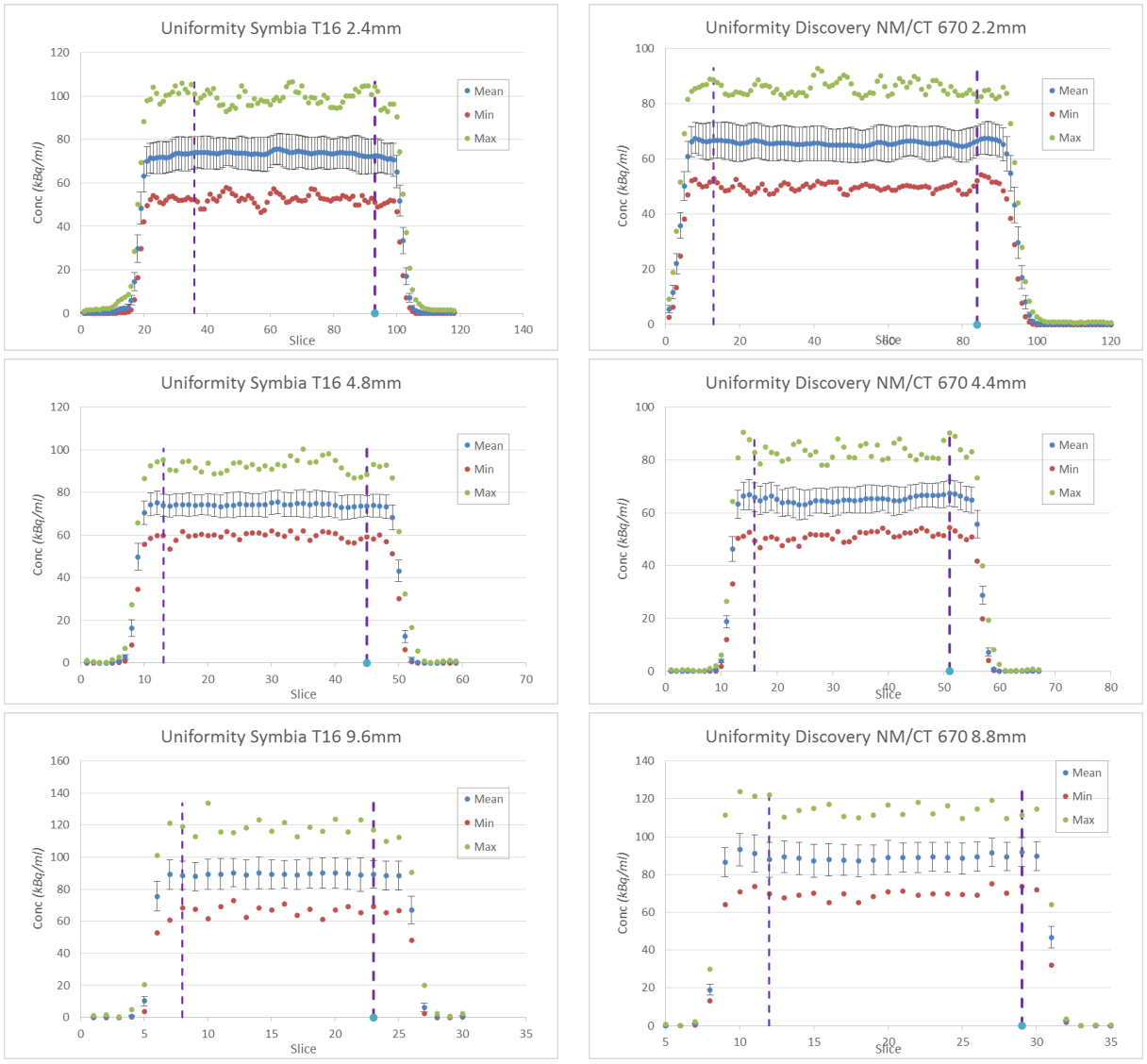

Figure 5.7: Uniformity analysis of both imaging systems at different pixel sizes. Left: Symbia T16. Right: Discovery NM/CT 670 (reconstructed with Hermes Hybridrecon)

Figure 5.8: Standard deviation analysis of both imaging systems at different pixel sizes. Left: Symbia T16. Right: Discovery NM/CT 670 (reconstructed with Hermes Hybridrecon)

There are small oscillation artefacts visible for the Symbia T16 (more visible at 2.2 mm).
There are oscillation artefacts visible for the Discovery NM/CT 670 (more visible at 2.2 mm).
The oscillations become heavier towards the bottom of the phantom.

5.2 Emission recovery coefficients

This section shows the results for the measurements with the NEMA IEC body phantom [28]. The images were reconstructed with Hermes Hybridrecon. The VOI's were drawn with Hermes Hybrid Viewer PDR 2.5A.
Figure 5.9 shows the emission recovery values for different sphere sizes for 3.3 mm, 4.8 mm and 9.6 mm pixels with varying updates from 4 to 120 for the Siemens Symbia T16.

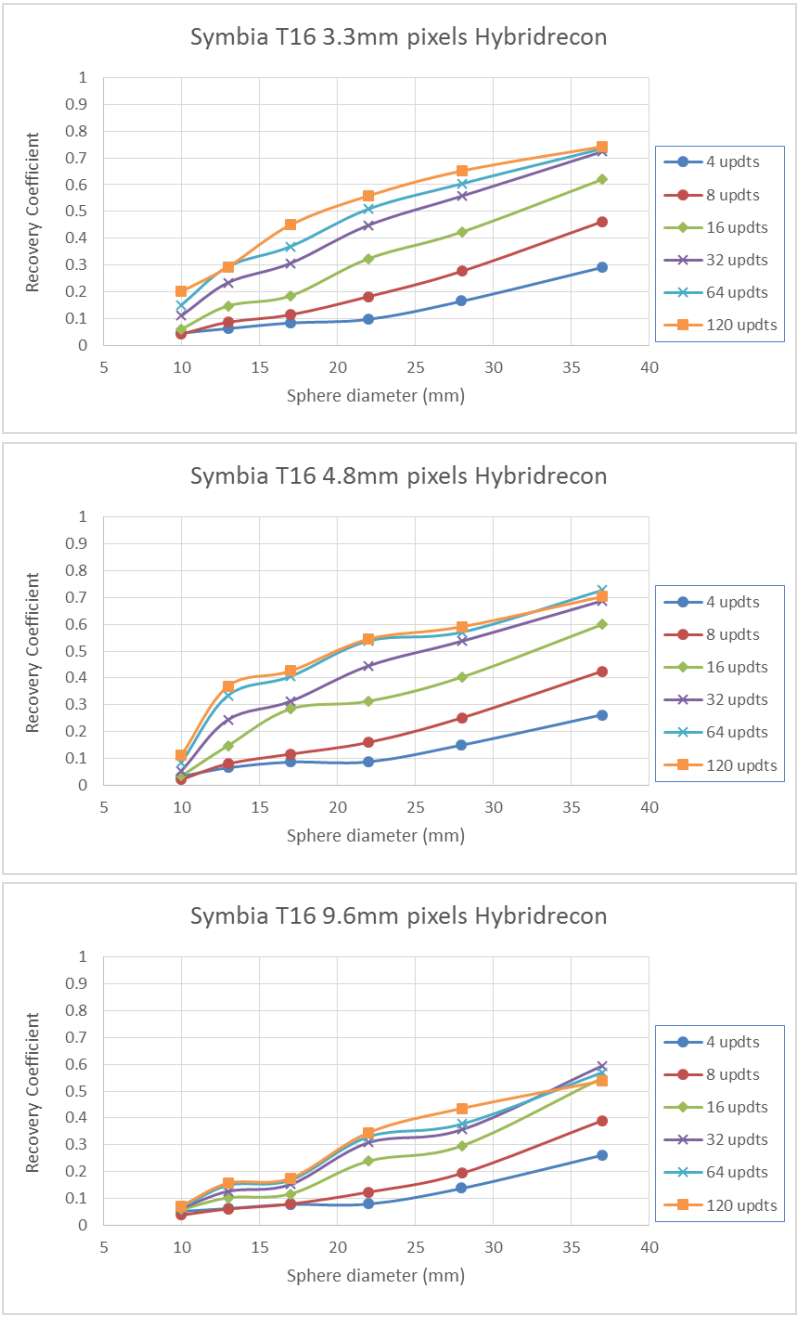

Figure 5.9: Recovery values for different object sizes for 3.3mm, 4.8mm and 9.6mm pixels with varying updates for Siemens Symbia T16 (Reconstructed wit Hermes Hybridrecon

At 3.3 mm pixels, the Recovery Value (RV) of the biggest sphere is 0.72 at 32 updates and 0.74 at 120 updates. For the smallest sphere, the RV drops to 0.10 at 32 updates and 0.20 at 120 updates. The recovery values seem so stabilize at 32 updates for the bigger spheres. At 4 updates, the RV of the smallest sphere drops below 0.045 and for the biggest sphere it reaches a value of 0.29.

At 4.8 mm pixels, the pattern is similar except that the RV's are twice as low than at 3.3 mm pixels. The RV is 0.68 for the biggest sphere and 0.05 for the smallest at 32 updates. At 4 updates, the RV of the smallest sphere drops below 0.035 and for the biggest sphere the RV is 0.11.

At 9.6 mm pixels, The RV's of the smallest spheres drop further with 20%. At 32 updates, The RV is 0.59 for the biggest sphere.

Figure 5.10 shows the emission recovery values for different sphere sizes for 2.9 mm, 4.4 mm and 8.8 mm pixels with varying updates from 4 to 120 for GE Discovery NM/CT 670.

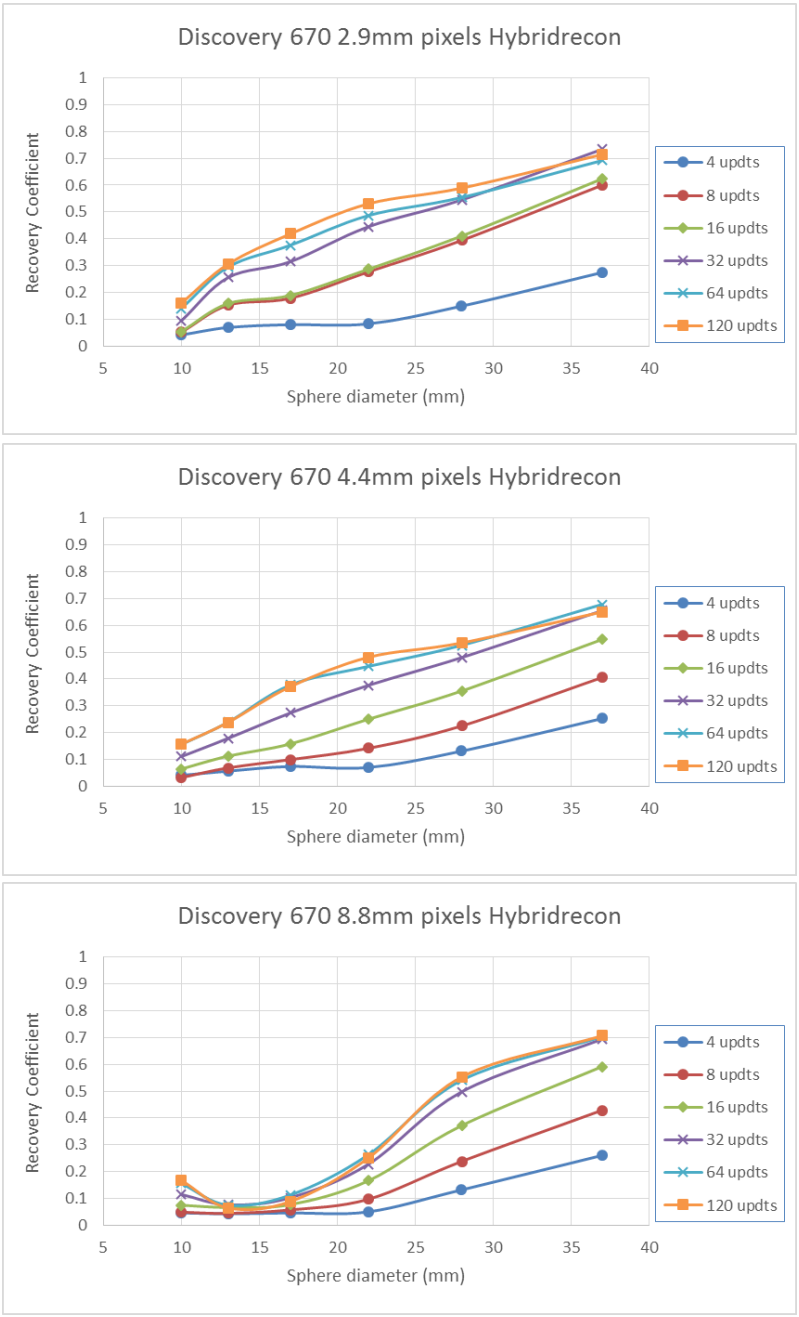

Figure 5.10: Recovery values for different object sizes for 2.9mm, 4.4mm and 8.8mm pixels with varying updates for GE Discovery NM/CT 670 (Reconstructed with Hermes Hybridrecon)

At 2.9 mm pixels, the recovery value (RV) of the biggest sphere is 0.73 at 32 updates and 0.71 at 120 updates. For the smallest sphere, the RV drops to 0.09 at 64 updates and 0.15 at 120 updates. The recovery values seem so stabilize at 32 updates. At 4 updates, the RV of the smallest sphere drops to 0.041 and for the biggest sphere it reaches a value of 0.27.
At 4.4 mm pixels, the pattern is similar except that the RV's are approximately 10% lower for the bigger spheres. The RV is 0.65 for the biggest sphere and 0.11 for the smallest. At 4 updates, the RV of the smallest sphere is 0.04 and for the biggest sphere the RV is 0.25.

At 8.83 mm pixels, The pattern is different. The RV's first drop with increasing sphere diameter but after 20 mm diameter they increase again. The lowest RV's are of the 13mm sphere. The RV is 0.69 for the biggest sphere.

5.2.1 Influence of activity

Figure 5.11 shows the RV's for the different spheres at different activities.

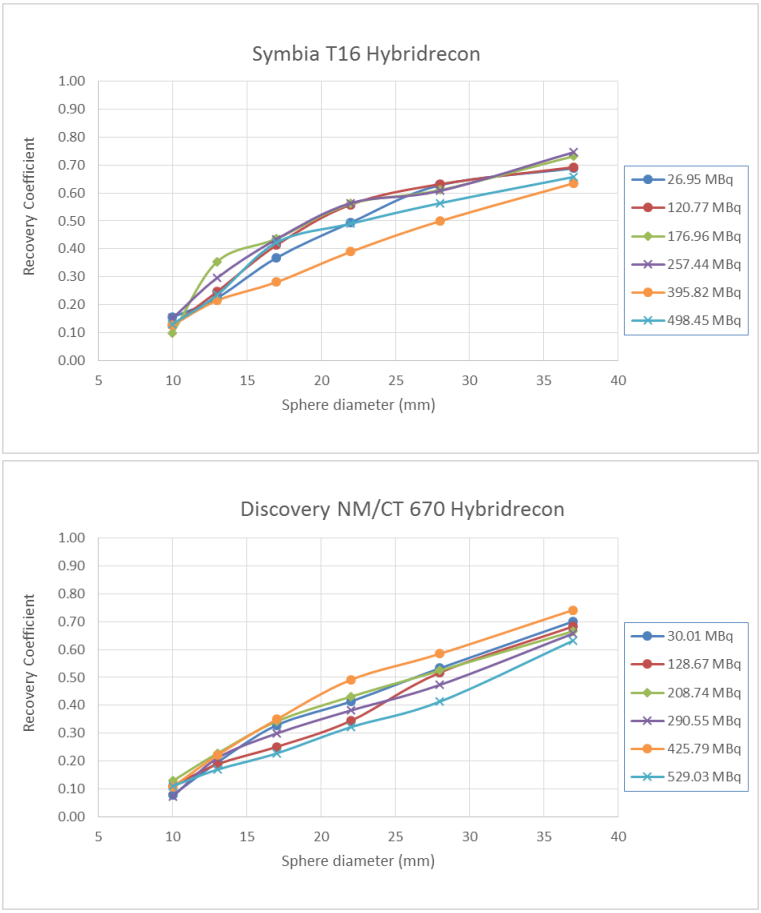

Figure 5.11: Recovery values in function of the sphere diameter at different activities (Hybridrecon)

For the Symbia T16, The RV's of the smallest sphere do not vary significantly. For the bigger spheres, the RV's first increase about 7% with increasing activity but after 300 MBq it drops with 12%. At ±400 MBq, the RV's converge slower with increasing sphere diameter.
For the Discovery NM/CT 670, again the RV's of the smallest spheres stay stable. For the bigger spheres, the RV's first drop with maximum 10% with increasing activity.

5.2.2 Effect of spill-in

Table 5.5 Shows the RV's of the lung insert (to measure the effect of spill-in) at different pixel sizes and varying updates and Figure 5.12 shows the RV's for the lung insert as a function of the pixel size for both imaging systems.

Table 5.5: Recovery values for the spill-in effect for different pixel sizes and varying updates of both imaging systems (Reconstructed with Hermes Hybridrecon).

Siemens Symbia T16

	Recovery values Spill-in					
Spill in (pixel size mm)	**4updts**	**8updts**	**16updts**	**32updts**	**64updts**	**120updts**
3.3	0.92	0.73	0.56	0.42	0.32	0.23
4.8	0.89	0.70	0.58	0.42	0.42	0.39
9.6	1.20	0.89	0.71	0.47	0.36	0.29

GE Discovery NM/CT 670

	Recovery values Spill-in					
Spill in (pixel size mm)	**4updts**	**8updts**	**16updts**	**32updts**	**64updts**	**120updts**
2.9	0.86	0.67	0.66	0.48	0.36	0.20
4.8	0.84	0.62	0.63	0.27	0.27	0.25
9.6	0.88	0.75	0.69	0.49	0.39	0.25

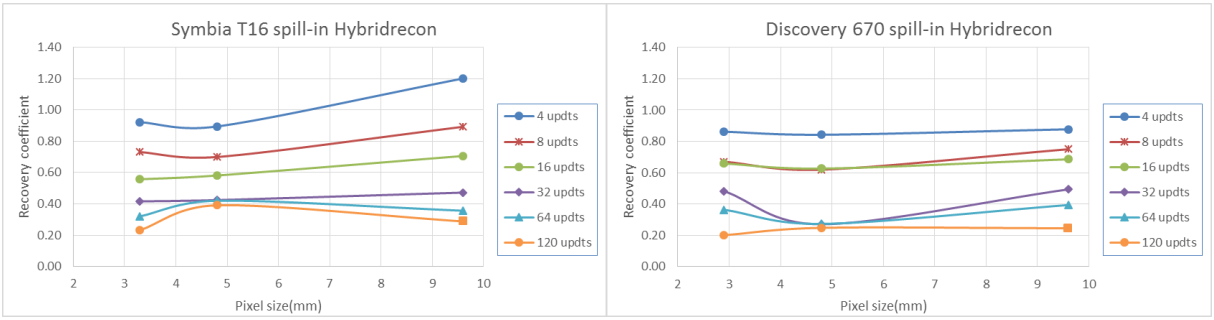

Figure 5.12: Effect of spill-in for different pixel sizes at varying updates from 4-120. Left: Siemens Symbia T16. Right: GE Discovery NM/CT 670 (Reconstructed with Hybridrecon)

The RV's drop with decreasing pixel size (except at 4 updates) and increasing updates but it stabilizes at 64 updates. At 4 updates and large pixel sizes, The RV's are around 100%. At 64 updates, the RV's are similar for different pixel sizes. At 120 updates, the RV's are still around 0.2.

6 Discussion

In this study the commercial algorithms were evaluated using attenuation, scatter correction and resolution recovery together. The imaging settings where chosen to be close to the clinical practice. This is the reason why a non-circular trajectory was used in most of the acquisitions because this is nowadays used in clinical practice to improve spatial resolution. The influence of basic parameters was investigated (updates, pixel size, activity) to determine the feasibility for quantification with SPECT/CT imaging for clinical Tc-99m.

6.1 Quantification

The System Volume Sensitivity (S_{vol}) is dependent on different factors like the radionuclide used, count rate, acquisition and reconstruction parameters and also the radionuclide calibrator used.
For example Zeintl et al. [27] reported a S_{vol} of 10.3 cpm/kBq for Siemens Symbia T16. Quantification for large bodies seems feasible within 4%. This means that the calibration factors obtained from the procedure in 3.4 could be used to calibrate the systems in absolute activity units (and possibly allowing to calculate SUV's for SPECT).
The influence of pixel size and detector motion and orbit is negligible considering the error of 4%. Except that the sensitivity seems to be slightly higher for Step-and-Shoot motion. The reason could be that with continuous motion, the camera still collects photons during rotation between projection angles and the projections are smoothed before being used. This could explain the loss of quantification.
The Siemens Symbia T16 seems to be (almost) twice as sensitive than the Discovery NM/CT 670. This could be caused by different physical parameters (e.g. PMT properties, collimator properties) and/or reconstruction algorithm. The influence of post-smoothing could also explain this. Flash3D uses a Gaussian post-smoothing function with a fixed value which can be changed by the user. This step is applied after the iteration loop. GE Evolution for Bone uses a MAP-EM algorithm which applies a penalty in each step to suppress noise. This option cannot be turned off. The lowest value which can be used is 0.1 pixels. The loss of quantification could be that in each step more and more noise is suppressed but this is in exchange to inferior sensitivity. A different value for the penalty step could improve sensitivity but also increase the noise. A compromise has to be made for this. Perhaps the initial bias of the iteration loop (first estimated image) is chosen in a way that it does not allow convergence even with many updates.
Flash3D makes 16 bit unsigned images whereas GE Evolution for Bone makes 16 bit signed images. This means the count range of Flash3D is twice than that from the GE Evolution. The GE Evolution for bone protocol contains a projection multiplication factor of 4. This is used for qualitative purposes where very low counts are multiplied to increase the dynamic range of the image. This gives better qualitative results (the images look better), but these images are not usable for quantification purposes. This was turned off for the acquisitions in this study. However, due to using signed images (lower count range), there could be other

"internal" scaling factors which could not be obtained without knowing the GE Evolution algorithm in more detail.
A small study was performed to examine the influence of different iteration combinations and post-smoothing for the Discovery NM/CT 670. The results are in Appendix B: In-depth analysis GE Discovery NM/CT 670. The results show that the post-smoothing has no effect on the sensitivity. The error decreases with increasing post-smoothing value. However, the cupping artefacts remain with all the different combinations. However, a more detailed study is needed to obtain a final conclusion. The results suggest that it is better to use post-smoothing because of the reduction in the error (certainly in diagnostic imaging were the activities are low and the images are very noisy).
The Hybridrecon algorithm with a Monte Carlo based scatter correction gives different results. This is different than the vendors algorithms which make use of additional scatter windows. The S_{vol} was 25% lower for the Symbia T16 and 15% higher for the Discovery NM/CT 670 (compared to the vendors algorithms). Hybridrecon takes physical information from different vendors (e.g. collimator, PMT characteristics) which they incorporate in their algorithm. It could be that the interpretation of count profiles with Hybridrecon is different than the vendors own algorithms, or the dynamic range which could be lower. This could introduce extra scaling factors which degrades quantification accuracy. On the SPECT images, it can be concluded that Hybridrecon uses a different implementation for the attenuation correction, because the metal stir rod was clearly visible on the SPECT images reconstructed with Hybridrecon whereas in the images constructed with the vendors algorithms the stir rod was invisible. Kangasmaa et al. [31] performed a multivendor analysis for the quantitative accuracy with the Hybridrecon algorithm. They made reconstructions with 10 iterations and 15-16 subsets with 0.8 mm Gaussian post-filtering. They calculated S_{vol} values for the Siemens Symbia T16 and GE Discovery NM/CT 670 of 9.53 cpm/kBq and 7.14 cpm/kBq respectively. The variations are probably related to the radionuclide calibrators used. They also concluded that quantification is feasible and repeatable.

Number of updates

The number of updates is the multiplication of the number of subsets with the number of iterations. In this study the updates were varied from 4-120 updates which is in the range used in clinical practice. Increasing the updates beyond 120 updates would not give interesting results because OSEM algorithms converges after a particular number of updates and the noise would keep increasing with more updates. The computation time would also increase considerably to the point where it would hinder clinical practice.
At few updates, the images won't converge to acceptable values and the effect of post-smoothing will be clearly visible. The images will look very blurry.
The S_{vol} shows the same pattern for both systems in function of the number of updates. The S_{vol} raises rapidly till 16 updates and after 32 updates it stabilizes to a constant value. The error also increases but slightly (probably because of the post-smoothing).
At 4 updates, the S_{vol} value of the Discovery NM/CT 670 is only 46% of the maximum value at higher updates whereas for the Symbia T16 the S_{vol} is 80% of the maximum value. This

means that the initial "guess" of the iteration process is closer to the convergence value for the Symbia T16. But, both systems converge at the same number of updates. The S_{vol} of the GE Discovery NM/CT 670 could be higher if the initial bias value is chosen higher.
For Hybridrecon, the S_{vol} converges at 8 updates and stabilizes at 16 updates. However there is loss of quantification. So Hybridrecon converges faster than the vendors algorithms but with the cost of loss of quantification. It could be that in order to decrease computation time, the used method introduces scaling factors to reach the maximum value faster. However this decreases quantitative accuracy. Perhaps some accelerating schemes are used where some values are "wrongly" estimated. The error also increases slightly with increasing updates because the noise also gets more reconstructed.
Based on these results it can be concluded that for accurate quantification the number of updates should be at least 32. The combination of the number of subsets and number of iterations should be further investigated. If the influence is minimal, an iteration scheme with many subsets and few updates could be used to speed up the iteration process. This would also increase the efficiency in clinical practice.

Activity

The activity during acquisition was varied between 20-500 MBq. Higher than 500 MBq seemed unnecessary because the detectors could reach saturation. Also such high activities of Tc-99m were not always available because the measurements were performed after the clinical practice. Besides, such high activities are not used for diagnostic clinical practice. Acquisitions with activities below 30 MBq were also performed because this is the activity range used in most diagnostic imaging modalities. This was prepared by injecting the phantom with a high activity the day before and letting it decay 24 hours. However to obtain good count statistics, the dwell time was increased to 30 seconds which gave a total scan time of 30 minutes. The error increased only slightly with the acquisition with low activity. This is probably due to the dwell time of 30 seconds which allowed for reliable count statistics. A dwell time of 10 seconds would give a much larger error. The S_{vol} value decreases slightly with increasing activity whereas the error decreases with increasing activity (which is expected). This is the same for both imaging systems and also for Hybridrecon. The reason that the sensitivity drops could be that the detectors reaches count rates that put them into saturation. Or that for low activities there is significantly more noise in the images which could be interpreted as normal image counts. However, The S_{vol} stays fairly stable for varying activities. This suggests that dosimetry for in vivo radionuclide therapies could be possible with this method.

Uniformity analysis

The uniformity analysis allows to examine physical artefacts like cupping and oscillation. Without attenuation correction, a large cupping artefact is clearly visible in the center of the phantom. The analysis was performed for each slice in the inner 80% of the phantom (because of Partial volume effects).

For Siemens Symbia T16, the uniformity stays fairly constant in the 80% of the phantom even for different updates or pixel sizes (also for the images with Hybridrecon).
With a scatter window of 15%, a large cupping artefact is visible in the center of the phantom. As the updates increased, the cupping artefact lessened but this time oscillation artefacts became visible. There is clearly under-correction in the center of the phantom. The oscillation artefacts are probably caused because of the penalty used in each step in the iteration loop for noise regularization. This problem could be solved by changing the scatter window parameters and/or the post-smoothing. The results from the small analysis in Appendix B show that the cupping artefact does not disappear when the post-smoothing value is changed. However the cupping artefact was less visible with a 10 % scatter window. Perhaps narrowing the scatter window even further could correct this artefact. But with such narrow windows the scatter correction won't be optimal because there will be considerably less photons detected in the scatter window.
For the Hybridrecon there are oscillation artefacts visible. This suggests that Hybridrecon also uses a MAP-EM algorithm to reconstruct images. Again by changing the post-smoothing or the energy window (for scatter correction) could solve this.

6.2 Contrast recovery

The NEMA IEC body phantom with 6 spheres with variable diameters and lung insert was used to examine the effect of spill-in and spill-out due to partial volume effects. The system resolution of a SPECT system is around 10 mm. The lung insert has a diameter of 44 mm and is used in this study to examine the influence of spill-in from the background. The 6 small spheres are used to examine spill-out to the background. In nuclear medicine, objects with sizes 2-3 times the system revolution are degraded because of partial volume effects. The images where acquired with a non-circular orbit to obtain maximum resolution recovery. The sphere to background ratio was approximately 10:1 in the images.
It should be noted that the study of the recovery values are operator dependent. Because operational errors could be introduced during the experiments. Also the VOI's are manually drawn which also introduces positional errors. The VOI's are translated from the CT image to the SPECT image, which could also introduces errors (depending on the software package used). The automatization of such studies where manually drawing of VOI's becomes obsolete would make contrast recovery analysis easier, more reliable and much faster. It is also important to consider that in these study the geometries were very simple, and the scanned object is not moving. The recovery values in more complex geometries could be different. The next step would be to examine the contrast recovery of small objects (e.g. small tumors) in patient studies where beside partial volume correction, a motion correction strategy would be necessary.
The recovery values for the smaller spheres are below 30%. This suggests that a partial volume correction strategy for these spheres is necessary (e.g. with segmentation of geometries obtained from the diagnostic CT-image). Otherwise, the activity will be severely underestimated (e.g. small tumors won't be visible on a SPECT image). Any method which increases the resolution of the SPECT images will also increase the recovery values for hot

spots. The RV's stabilize at 64 updates. Kangasmaa et al. [31] obtained very similar results for the RV's (both Symbia T16 and Discovery NM/CT 670) with the NEMA IEC phantom. They used a Sphere/Background ratio of 8:1. The influence of the Sphere/Background ratio should be further investigated. Perhaps a new method should be developed to make such analysis more repeatable.

The RV's for the GE Discovery 670 for the bigger spheres are 10% higher. This could come because of the MAP-EM algorithm. It could be that this algorithm is more optimized for contrast recovery than for quantification. Because at each step the noise is suppressed which improves the contrast recovery. However over-suppressing the noise in each image degrades the sensitivity.

At large pixels, the spill-in from the background to the lung insert is even higher than 100% for low updates. Even for 120 updates, there is still a recovery coefficient of 20% for the spill-in. The reason could be that OS-EM does not converge to a "zero" likely. The initial guess is mostly a uniform concentration and even with many updates this does not converge fully. The next step should be to study the effect of spill-in for objects of different diameters and different shapes.

At different activities, the RV's do not vary significantly (even with very low activities). This suggests that a correction strategy for partial volume artefacts could be applied to images in all activity ranges. It should be noted that in this study all acquisitions with the NEMA phantom had a sphere/background ratio of approximately 10:1. Different ratios could give different results.

7 Reflection

This chapter deals with the personal reflections and experiences during the internship:

- Measuring activities with the radionuclide calibrator proved to be a major challenge. It required a great amount of dexterity and patience to draw out the right amount of activity in the syringe. Besides, the user must operate very carefully to not contaminate himself/herself and the near environment.
- It was not easy to fill an empty cylinder completely with demineralised water. It was very difficult to get all the air bubbles out of it.
- Cleaning the spheres of the NEMA phantom was extremely difficult. Especially in the small spheres. Sometimes little droplets remained inside the biggest spheres. This slightly decreased the accuracy of the measurements.
- The preparation of the NEMA phantom took around 30 minutes. The preparation of the activity concentrations for the background and spheres took a considerable time.
- Placing the phantoms parallel on the patient bed is not very easy. Sometimes this took around 10 minutes to ensure that the phantom was placed perfectly.
- All the measurements were performed in the late evening after the clinical practice. Some days the measurements were performed after 6 pm.
- Because the research was done with liquid radioactive sources, patience and caution were obligatory to ensure there was no contamination.
- The operation of Discovery NM/CT 670 was slightly easier and faster. There were some shortcut buttons to ensure a faster placement of the phantom.
- However, the operation of the Syngo 2009A workstation was faster and easier than the Xeleris 3.0 workstation. The Syngo 2009A workstation is a integrated system were you can acquire and reconstruct images in one step. The reconstructions were also faster with the Flash3D algorithm.
- The Xeleris 3.0 requires 2 different steps to acquire and reconstruct images. The reconstruction time was also longer.
- During the internship there was an upgrade to Xeleris 3.1. The iteration process seemed a little faster. The User Interface (UI) didn’t change much.

8 Conclusion

Both SPECT-CT systems achieved quantitative accuracy within 4% for large objects even for very low activities. Quantification seems feasible for activities used in diagnostic imaging. The calculated Calibration Factors (CF) can be used for SUV analysis. The number of updates should be at least 32 for accurate results. The calibration method in this study could possibly be used in clinical practice to perform radionuclide uptake analysis and SUV analysis. The GE Evolution for Bone protocol should be optimized to reduce cupping and oscillation artefacts.

A partial volume correction strategy remains necessary for the smallest objects. The effect of spill-in should be further investigated for different geometries and sizes. The improvement of the system resolution will decrease partial volume effects. Improving the iteration algorithms to take into account Partial Volume Effects is crucial for Q-SPECT. Also, new algorithms which automate the VOI analysis (especially for NEMA phantom analysis) will increase the accuracy and speed up the process to Q-SPECT.

The influence of reconstruction artefacts remain a challenge for quantitative SPECT and should be the focus of further research. The reduction of the influence of these artefacts will bring in vivo dosimetry with SPECT imaging one step closer.

References

[1] J. Zeintl, “Optimizing Application Driven Multimodality Spatio-Temporal Emission Imaging,” Universitât Erlangen-Nürnberg, 2011.

[2] P. Ritt, H. Vija, J. Hornegger, and T. Kuwert, “Absolute quantification in SPECT,” *Eur. J. Nucl. Med. Mol. Imaging*, vol. 38, no. SUPPL. 1, pp. 69–77, 2011.

[3] H. Ahmadzadehfar and H. J. Biersack, *Clinical applications of SPECT-CT*. 2014.

[4] S. Fanti, M. Farsad, and L. Mansi, “Dosimetry Using SPECT-CT,” in *Atlas of SPECT-CT*, Heidelberg-Berlin, 2011, pp. 213–224.

[5] P. Ritt, J. Sanders, and T. Kuwert, “SPECT/CT technology,” *Clin. Transl. Imaging*, vol. 2, no. 6, pp. 445–457, 2014.

[6] D. W. Jones, P. Hogg, and E. Seeram, *Practical SPECT/CT in Nuclear Medicine*. Springer, 2013.

[7] Cyberphysics, “The Gamma Camera,” 2016. [Online]. Available: http://www.cyberphysics.co.uk/topics/radioact/gammaCamera.html. [Accessed: 22-Mar-2016].

[8] G. Saha, *Physics and Radiobiology of nuclear medicine*, vol. 53, no. 9. USA: Springer, 2013.

[9] J. Greenfield and Davis, “Detectors - Chemwiki,” 2016. [Online]. Available: http://chemwiki.ucdavis.edu/Analytical_Chemistry/Instrumental_Analysis/Spectrometer/Detectors/Detectors. [Accessed: 22-Mar-2016].

[10] G. Ebel and T. Aspelmeier, *Imaging in Nuclear Medicine*. Springer, 2013.

[11] D. Delbeke and O. Israel, *Hybrid PET/CT and SPECT/CT imaging*, vol. 53, no. 9. New York, 2013.

[12] M. Lyunberg, “Quantitative Spect Imaging,” in *Basic Sciences of Nuclear Medicine*, Springer, 2011, pp. 285–309.

[13] L. A. Shepp and Y. Vardi, “Maximum Likelihood Reconstruction for Emission Tomography,” *IEEE Trans. Med. Imaging*, vol. 1, no. 2, pp. 113–122, Oct. 1982.

[14] IAEA, *Nuclear Medicine Physics.*, vol. 38, no. 8. 2011.

[15] H. M. Hudson and R. S. Larkin, “Accelerated image reconstruction using ordered subsets of projection data,” *IEEE Trans. Med. Imaging*, vol. 13, no. 4, pp. 601–609, 1994.

[16] Fleming, “a technique for using ct images in attenuation corr.pdf,” *Nucl. Med. Commun.*, vol. 10, pp. 83–97, 1989.

[17] R. J. Jaszczak, C. E. Floyd, and R. E. Coleman, “Scatter compensation techniques for spect,” *IEEE Trans. Nucl. Sci.*, vol. 32, no. 1, pp. 786–793, 1985.

[18] T. Ichihara, K. Ogawa, N. Motomura, A. Kubo, and S. Hashimoto, “Compton Scatter Compensation Using the Dual-Isotope SPECT,” vol. 34, no. 12, pp. 2216–2221, 2014.

[19] A. Sohlberg, H. Watabe, and H. Iida, “Acceleration of Monte Carlo-based scatter compensation for cardiac SPECT.,” *Phys. Med. Biol.*, vol. 53, no. 14, pp. N277–N285, 2008.

[20] B. F. Hutton, I. Buvat, and F. J. Beekman, “Review and current status of SPECT scatter correction.,” *Phys. Med. Biol.*, vol. 56, pp. R85–R112, 2011.

[21] A. V. Bronnikov, “SPECT imaging with resolution recovery,” *IEEE Trans. Nucl. Sci.*, vol. 59, no. 4 PART 2, pp. 1458–1464, 2012.

[22] A. Seret, D. Nguyen, and C. Bernard, “Quantitative capabilities of four state-of-the-art SPECT-CT cameras,” *EJNMMI Res.*, vol. 2, p. 45, 2012.

[23] E. C. Frey and B. M. W. Tsui, “A new method for modeling the spatially-variant, object-dependent\nscatter response function in SPECT,” *1996 IEEE Nucl. Sci. Symp. Conf. Rec.*, vol. 2, pp. 1082–1086, 1996.

[24] E. C. Frey and B. M. W. Tsui, “Collimator-detector response compensation in SPECT,” pp. 141–166, 2006.

[25] Chuanyong Bai, Gengsheng L. Zeng, G. T. Gullberg, F. DiFilippo, and S. Miller, “Slab-by-slab blurring model for geometric point response correction\nand attenuation correction using iterative reconstruction\nalgorithms,” *IEEE Trans. Nucl. Sci.*, vol. 45, no. 4, pp. 2168–2173, 1998.

[26] P. J. Green, “Bayesian reconstructions from emission tomography data using a modified EM algorithm.,” *IEEE Trans. Med. Imaging*, vol. 9, no. 1, pp. 84–93, 1990.

[27] J. Zeintl, A. H. Vija, A. Yahil, J. Hornegger, and T. Kuwert, “Quantitative accuracy of clinical 99mTc SPECT/CT using ordered-subset expectation maximization with 3-dimensional resolution recovery, attenuation, and scatter correction.,” *J. Nucl. Med.*, vol. 51, no. 6, pp. 921–928, 2010.

[28] “NEMA IEC Body Phantom Set ™,” 2001. [Online]. Available: http://www.spect.com/pub/NEMA_IEC_Body_Phantom_Set.pdf.

[29] G. Schramm, M. Koole, B. Vanbilloen, E. D’Hoe, K. Vunckx, and J. Nuyts, “31st BHPA Symposium ur goal is expertise Liège , 26-27 February 2016 BHPA 2016 ABSTRACT SUBMISSION FORM Name : First name : Calibration 31st BHPA Symposium ur goal is expertise Liège , 26-27 February 2016,” in *Results of a NEMA PET image quality measurement in the GE SIGNA time-of-flight PET/MRI*, 2016, no. M, pp. 26–27.

[30] F. Hofheinz, S. Dittrich, C. Pötzsch, and J. Van Den Hoff, “Effects of cold sphere walls in PET phantom measurements on the volume reproducing threshold,” *Phys. Med. Biol.*, vol. 55, no. 4, pp. 1099–1113, 2010.

[31] T. S. Kangasmaa, C. Constanble, E. Hippeläinen, and A. O. Sohlberg, “Multicenter evalutation of single-photon emission computed tomography quantification with third-party reconstruction software,” *Nucl. Med. Commun.*, vol. 0, no. 0, pp. 1–5, 2016.

Appendix A: Well counter results

The counts per minute (cpm) obtained from the well counter were used to calibrate the System Volume Sensitivity (S_{vol}) of the 1 ml samples. First, the decay corrected count rate was calculated with Equation (1) and then the S_{vol} was calculated with Equation (2).

The mean S_{vol} value of all the samples were (46257 ± 1700) cpm/kBq. Figure 1 shows the deviation to the mean of the Svol values.

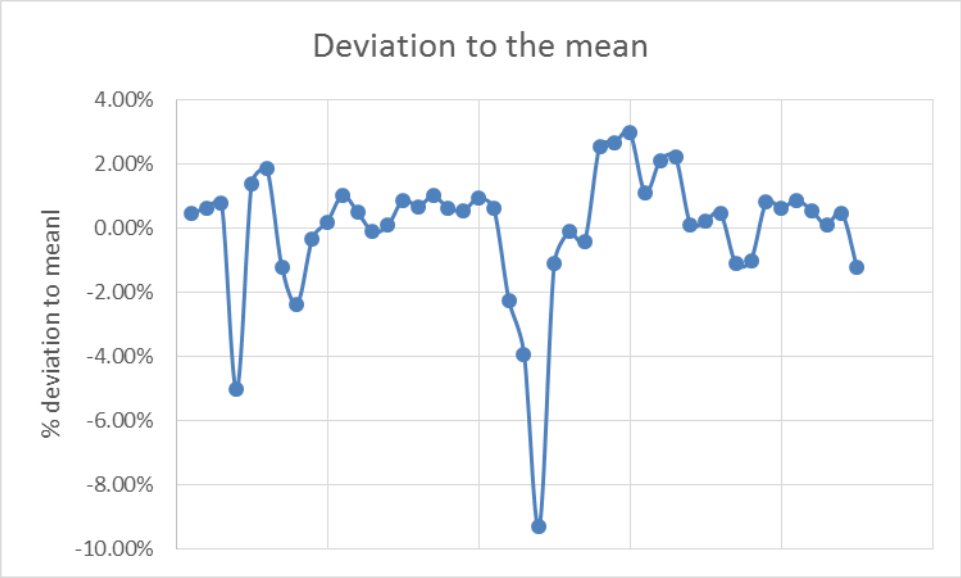

Figure 1: Deviation to the mean of the S_{vol} of the 1ml samples. The 2 samples with more than 5% deviation are due to preparation errors of the samples.

Appendix B: In-depth analysis GE Discovery NM/CT 670

The influence of post-smoothing was analysed on the Discovery NM/CT 670 by making reconstructions with different iteration combinations and different post-smoothing values (from the acquisition of the uniform cylindrical phantom). The same reconstructions were also made with Hermes Hybridrecon. It is important to note that on the Xeleris workstation it is not possible to totally disable the post-smoothing. If the value is set to "0 pixels", than the software automatically interprets this as "4.0 pixels" post-smoothing. Instead, 0.1 pixels post-smoothing was used.

The S_{vol} is the same with different iteration combinations and post-smoothing. However, the error decreases from 7 % (with 0.1 pixels post-smoothing) to 4% (with 4 pixels post-smoothing).
Figure 1 and figure 2 show the uniformity analysis with post-smoothing of 0.1 pixels and 4 pixels respectively. Figure 3 and figure 4 show the standard deviation analysis with post-smoothing of 0.1 pixels and 4 pixels respectively. The purple dashed lines represent the inner 80 % of the phantom.

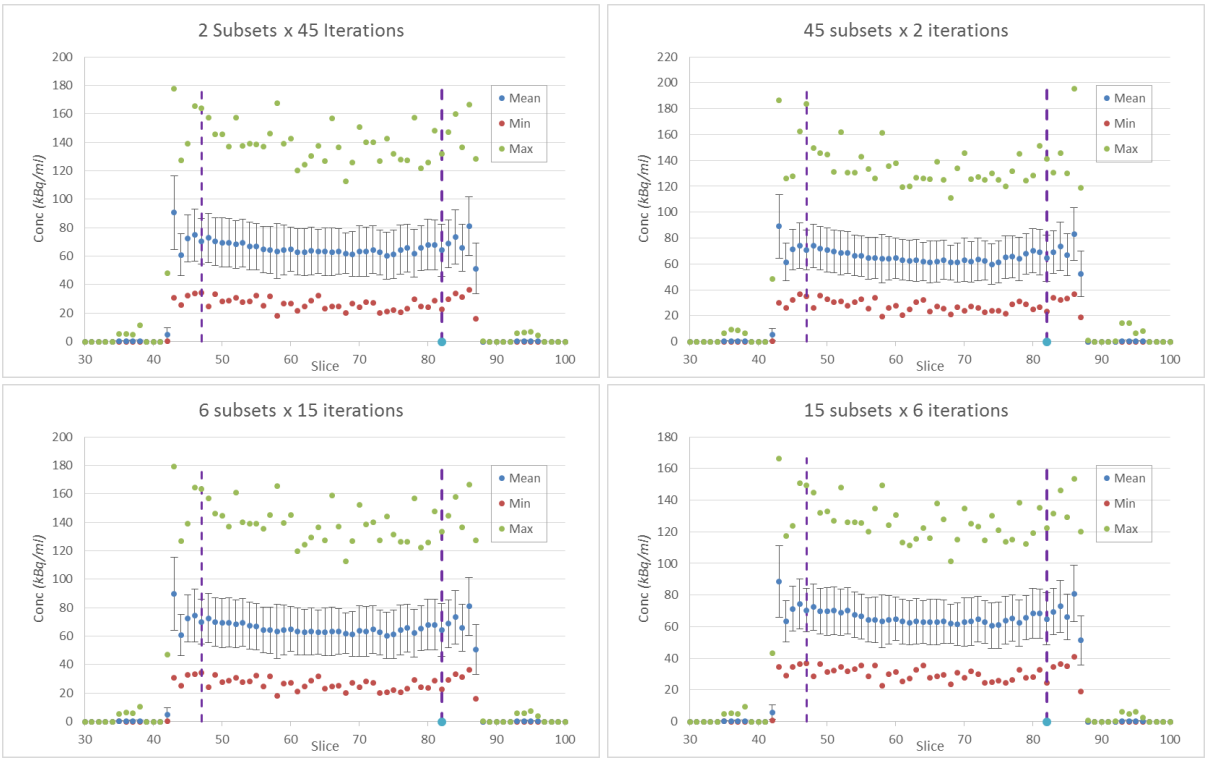

Figure 1: Uniformity analysis for different iteration combinations with 0.1 pixels post-smoothing.

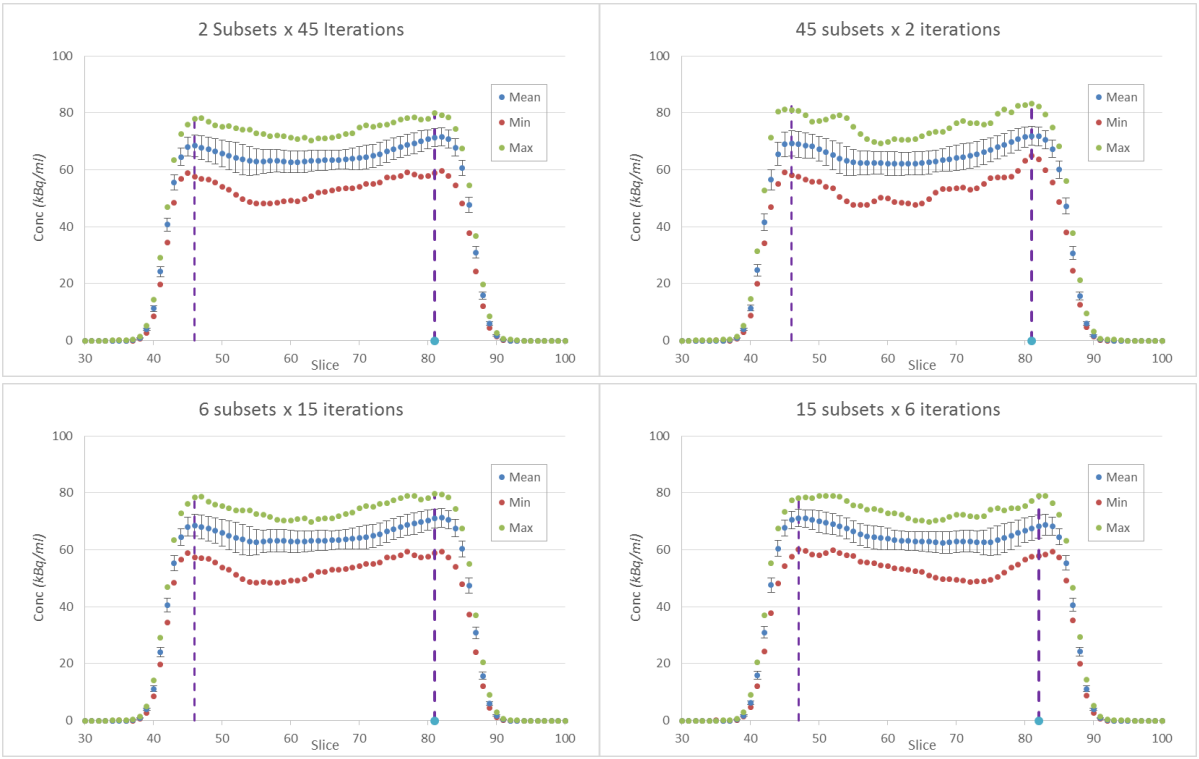

Figure 2: Uniformity analysis for different iteration combinations with 4 pixels post-smoothing.

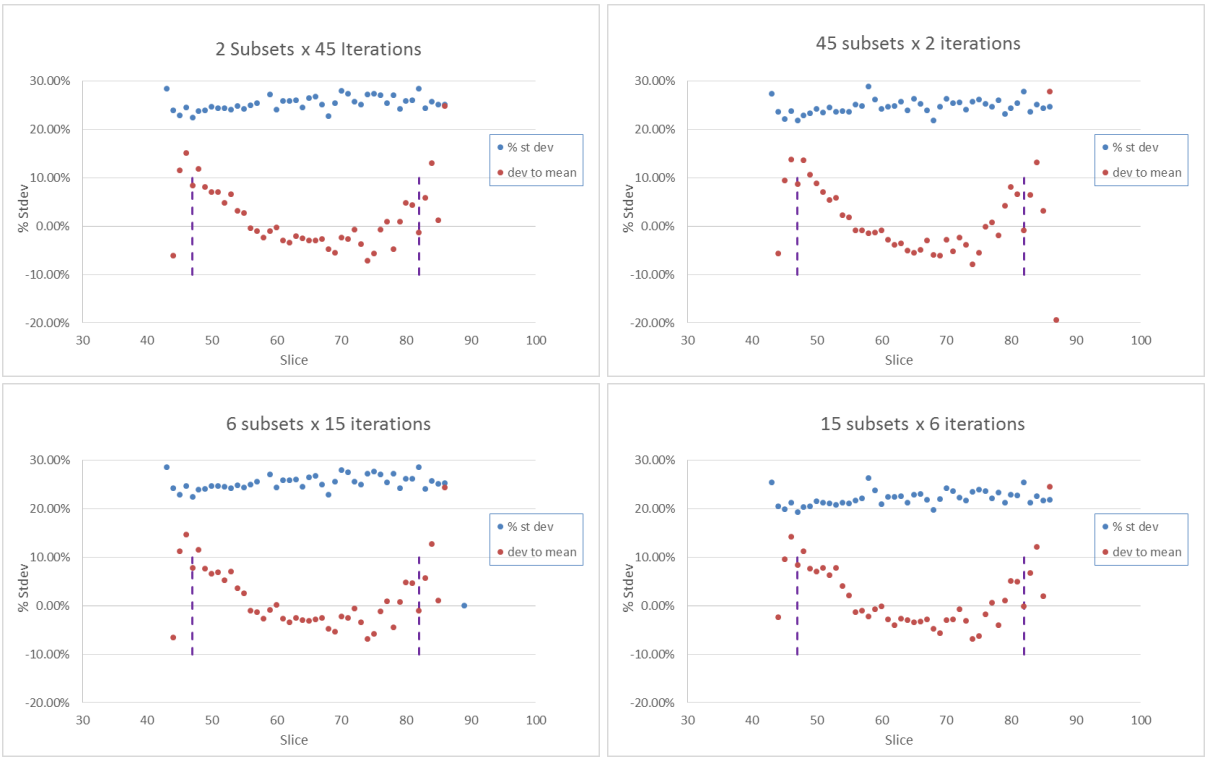

Figure 3: Standard deviation analysis for different iteration combinations with 0.1 pixels post-smoothing.

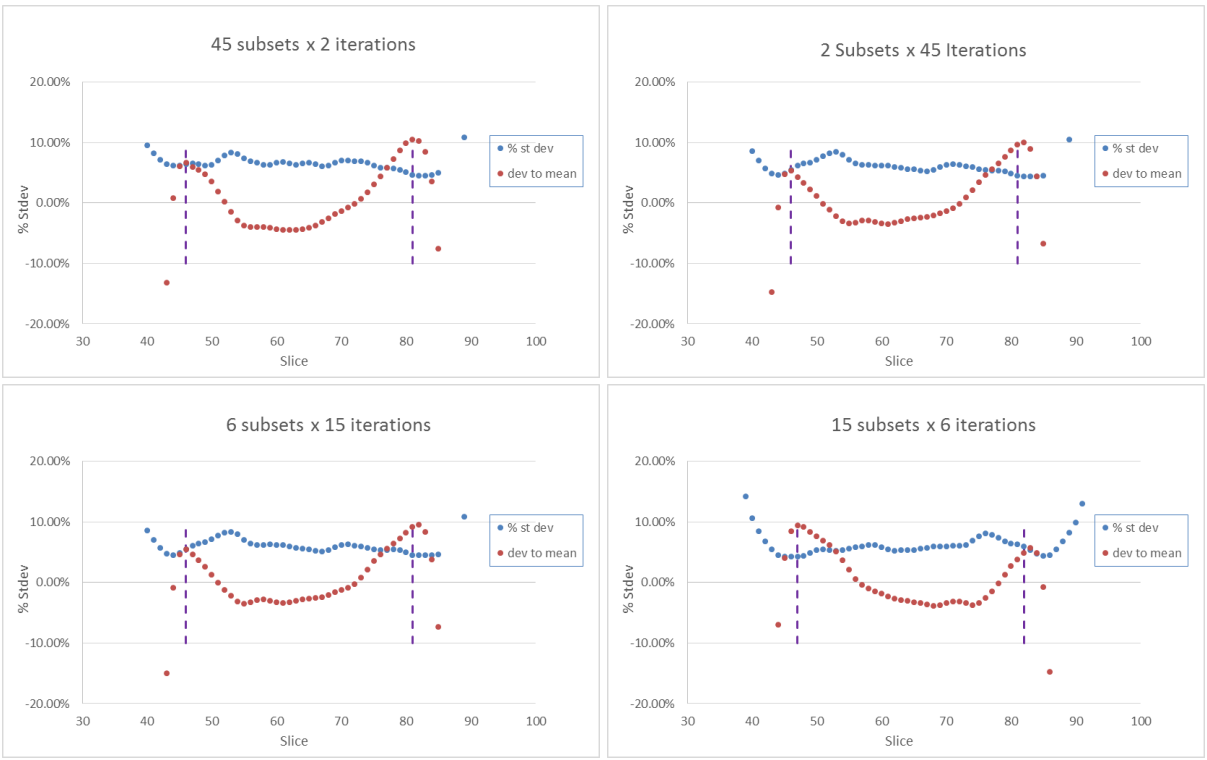

Figure 4: Standard deviation analysis for different iteration combinations with 4 pixels post-smoothing.

The standard deviation is 3 times higher with 0.1 pixels post-smoothing than with 4 mm post-smoothing. There is no variation with the different iteration combinations. The cupping artefact remains even with 0.1 pixels post-smoothing.

Hybridrecon

It is important to notice that the Hybridrecon algorithm does not allow to use more updates and/or iterations than 32. However, it is possible to totally disable the post-smoothing.

The S_{vol} is the same with different iteration combinations and post-smoothing. However, the error decreases from 7 % (with no post-smoothing) to 4% (with 4 pixels post-smoothing).

Figure 5 and figure 6 show the uniformity analysis with no post-smoothing and 4 pixels respectively. Figure 7 and figure 8 show the standard deviation analysis with no post-smoothing and 4 pixels respectively. The purple dashed lines represent the inner 80 % of the phantom.

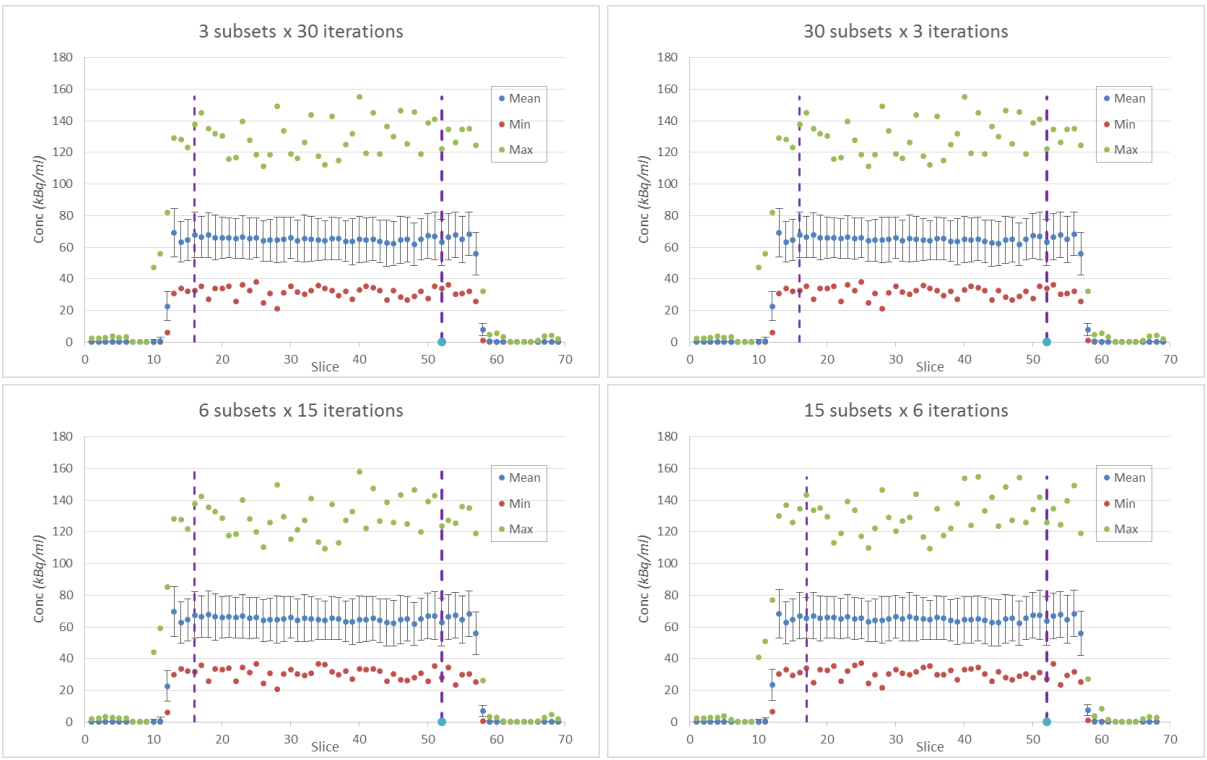

Figure 5: Uniformity analysis for different iteration combinations with no post-smoothing (Reconstructed with Hermes Hybridrecon)

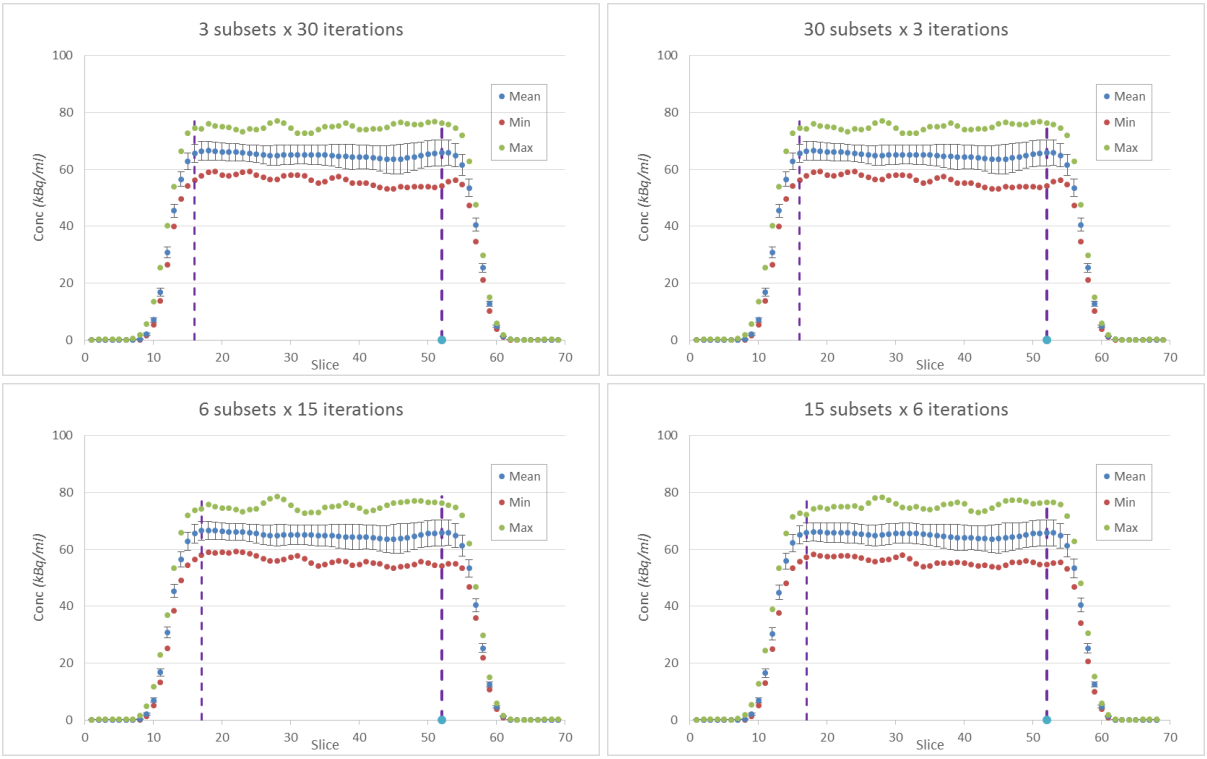

Figure 6: Uniformity analysis for different iteration combinations with 4 pixels post-smoothing (Reconstructed with Hermes Hybridrecon)

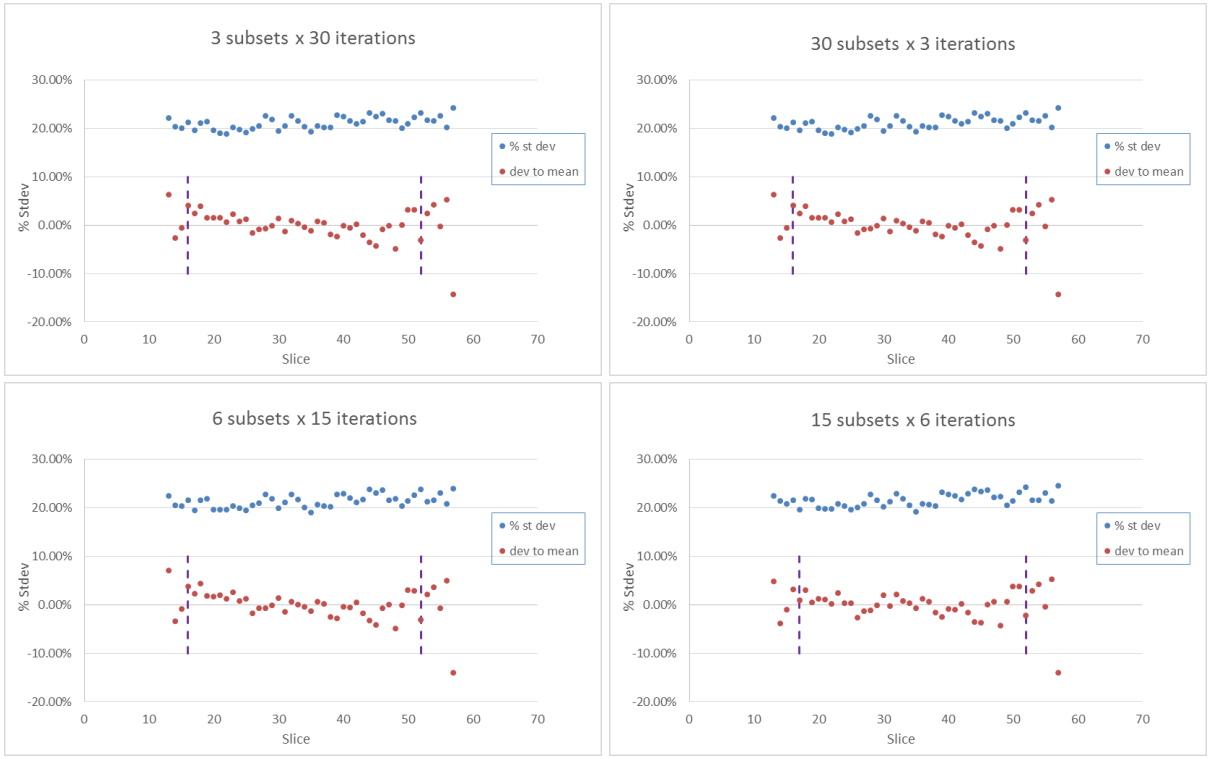

Figure 7: Standard deviation analysis for different iteration combinations with no post-smoothing (Reconstructed with Hermes Hybridrecon)

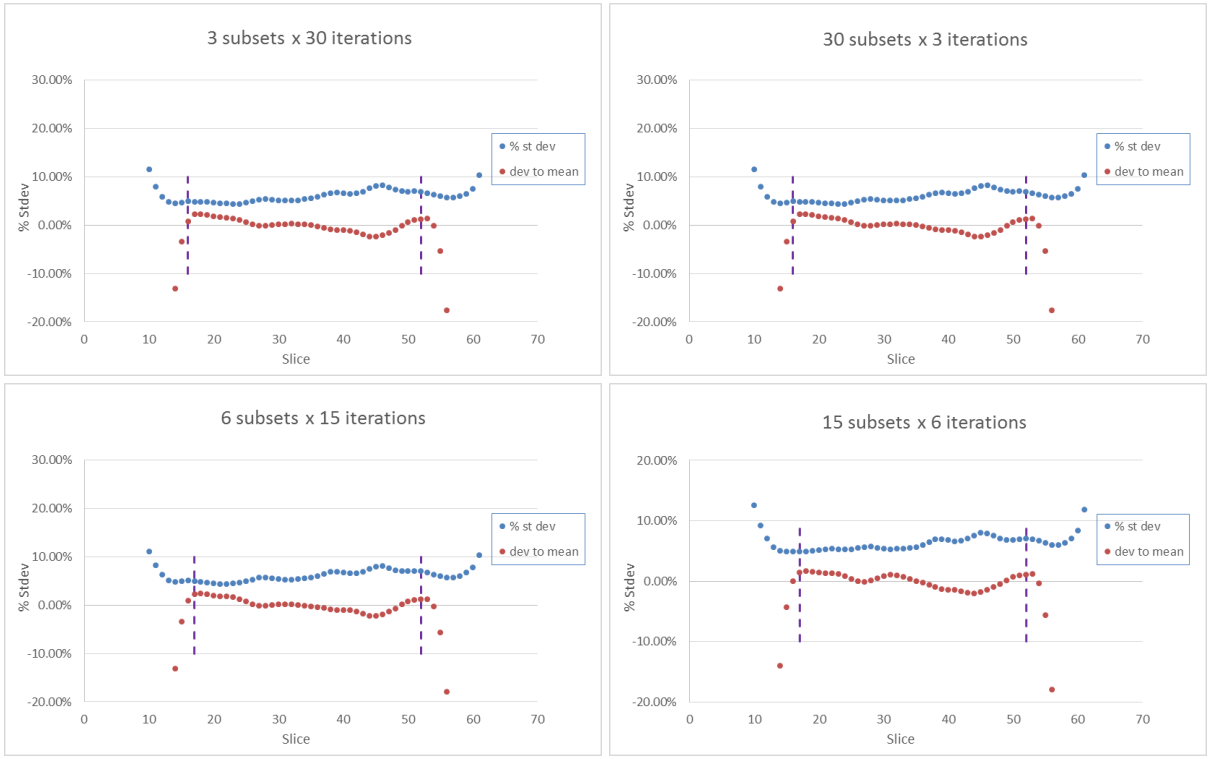

Figure 8: Standard deviation analysis for different iteration combinations with 4 pixels post-smoothing (Reconstructed with Hermes Hybridrecon)

The standard deviation is two times higher with no post-smoothing than with 4 pixels post-smoothing. There is no variation with the different iteration combinations. The oscillation artefacts remain.

Auteursrechtelijke overeenkomst

Ik/wij verlenen het wereldwijde auteursrecht voor de ingediende eindverhandeling:
Quantitative capabilities of 2 state-of-the-art SPECT/CT imaging systems

Richting: **master in de industriële wetenschappen: nucleaire technologie-nucleaire technieken / medisch nucleaire technieken**
Jaar: **2016**

in alle mogelijke mediaformaten, - bestaande en in de toekomst te ontwikkelen - , aan de Universiteit Hasselt.

Niet tegenstaand deze toekenning van het auteursrecht aan de Universiteit Hasselt behoud ik als auteur het recht om de eindverhandeling, - in zijn geheel of gedeeltelijk -, vrij te reproduceren, (her)publiceren of distribueren zonder de toelating te moeten verkrijgen van de Universiteit Hasselt.

Ik bevestig dat de eindverhandeling mijn origineel werk is, en dat ik het recht heb om de rechten te verlenen die in deze overeenkomst worden beschreven. Ik verklaar tevens dat de eindverhandeling, naar mijn weten, het auteursrecht van anderen niet overtreedt.

Ik verklaar tevens dat ik voor het materiaal in de eindverhandeling dat beschermd wordt door het auteursrecht, de nodige toelatingen heb verkregen zodat ik deze ook aan de Universiteit Hasselt kan overdragen en dat dit duidelijk in de tekst en inhoud van de eindverhandeling werd genotificeerd.

Universiteit Hasselt zal mij als auteur(s) van de eindverhandeling identificeren en zal geen wijzigingen aanbrengen aan de eindverhandeling, uitgezonderd deze toegelaten door deze overeenkomst.

Voor akkoord,

Yalvac, Burak

Datum: **30/05/2016**